Quaternary Research (2023), **114**, 114–129
doi:10.1017/qua.2023.5

Research Article

Geophysical sediment properties of a late Pleistocene loess–paleosol sequence, Chenarli, northeastern Iran

Amin Ghafarpour[a], Farhad Khormali[a]*, Hossein Tazikeh[a], Martin Kehl[b], Christian Rolf[c], Manfred Frechen[c] and Christian Zeeden[c]

[a]Department of Soil Sciences, Loess Research Center, Gorgan University of Agricultural Sciences and Natural Resources, Gorgan, Iran; [b]Institute of Geography, University of Cologne, Albertus-Magnus-Platz, 50923, Cologne, Germany and [c]Leibniz Institute for Applied Geophysics (LIAG), Stilleweg 2, 30655, Hanover, Germany

Abstract

We present stratigraphic, magnetic, diffuse reflectance spectrophotometric analyses, and chronologic data for the Chenarli loess–paleosol sequence in northeastern Iran. Eight loess units (LU) are identified, described, and constrained in time based on relative stratigraphy and luminescence dating from >130 ± 9.1 ka to ~9.8 ± 0.7 ka. Our data indicate that pedogenic magnetite/maghemite formation gives rise to magnetic enhancement in modern soil and paleosols. The top of LU 7 is demarcated by the well-developed last interglacial soil in which magnetic depletion occurred. We infer that magnetic depletion in this paleosol was produced by reducing conditions in a seasonally waterlogged soil during a warm and wet phase within Marine Isotope Stage (MIS) 5e. Units LU 6 to 1 record several episodes of dust accumulation and soil formation during the last glacial and Holocene. Increased dust accumulation rates occurred during middle-late MIS 3 and lasted into the late MIS 2, with a peak during the last glacial maximum (LU 2). These findings could be applicable to understanding magnetic enhancement/dissolution mechanism in the loess–paleosol sequences in study area. We infer paleoenvironmental changes in northeastern Iran relative to northern Iran, Eurasia, and China.

Keywords: Magnetic measurements, Northern Iranian loess plateau, Paleosols, Luminescence dating, Paleoclimate

(Received 28 January 2022; accepted 23 January 2023)

INTRODUCTION

Loess–paleosol sequences in mid- to high-latitude regions reflect a changing balance between pedogenesis and loess accumulation (e.g., Heller and Liu, 1984; Catt, 1991; Pecsi, 1995; Begét, 2001; Schaetzl et al., 2018; Rousseau et al., 2020; Song et al., 2021). Extensive loess deposits are found in northern and northeastern Iran, especially in the northern Iranian Loess Plateau (NILP) and along the northern foothills of the Alborz Mountains (NFAM; Fig. 1). These loess deposits are separated by buried soils that formed under relatively moist and warm climatic conditions (e.g., Frechen et al., 2009; Kehl, 2010; Karimi et al., 2011; Lauer et al., 2017b; Ghafarpour et al., 2021a; Kehl et al., 2021). Regressions and transgressions of the Caspian Sea (e.g., Yanina, 2014; Yanina et al., 2018; Krijgsman et al., 2019; Leroy et al., 2020) may have affected loess formation in the Caspian Lowlands by changing the size of the dust source area and by their influence on regional climate (Vlaminck et al., 2018; Kehl et al., 2021). Little information is available on the origin of loess in the area. Ghafarpour et al. (2021b) pointed out that loess in the Mobarakabad section in the NFAM may have originated from actively eroding crustal sources from relatively young mountain belts (Alborz and Kopet Dagh) around the loess accumulation area. Furthermore, Költringer et al. (2022) proposed a complex system for the primary sources and transportation pathways of loess at Aghband in the NILP, including sediments of the South Caspian Basin, the Karakum Desert, and nearby and distant mountain ranges.

Diffuse reflectance spectrophotometry (DRS) provides a rapid, nondestructive, and quantitative method to identify the iron oxide and oxyhydroxide minerals hematite and goethite (e.g., Balsam and Deaton, 1991; Torrent et al., 2007; Hu et al., 2016; Sandeep et al., 2017). DRS has been applied to loess–paleosol sequences to understand pedogenic processes and to reconstruct past climate (Ji et al., 2002; Balsam et al., 2004; Hu et al., 2013; Zeeden et al., 2017; Laag et al., 2021). Magnetic measurements provide information on magnetic enhancement/dissolution mechanisms in soils and paleosols (e.g., Geiss et al., 2008; Orgeira et al., 2011; Roberts, 2015; Ahmed and Maher, 2018; Bilardello et al., 2020) and can be used to quantify soil and paleosol development intensity (e.g., Spassov et al., 2003; Geiss and Zanner, 2006; Tecsa et al., 2020; Költringer et al., 2021). Magnetic properties have also been widely used to reconstruct paleoclimate changes in loess–paleosol sequences (e.g., Hu et al., 2015; Zeeden et al., 2018; Stevens et al., 2020; Bradák et al., 2021; Wacha et al., 2021). Previous studies of loess–paleosol sequences in northern and northeastern Iran have shown that modern soils and

*Corresponding author at: Department of Soil Sciences, Loess Research Center, Gorgan University of Agricultural Sciences and Natural Resources, Gorgan, Iran. E-mail address: fkhormali@gau.ac.ir; khormali@yahoo.com (F. Khormali)

Cite this article: Ghafarpour A, Khormali F, Tazikeh H, Kehl M, Rolf C, Frechen M, Zeeden C (2023). Geophysical sediment properties of a late Pleistocene loess–paleosol sequence, Chenarli, northeastern Iran. *Quaternary Research* **114**, 114–129. https://doi.org/10.1017/qua.2023.5

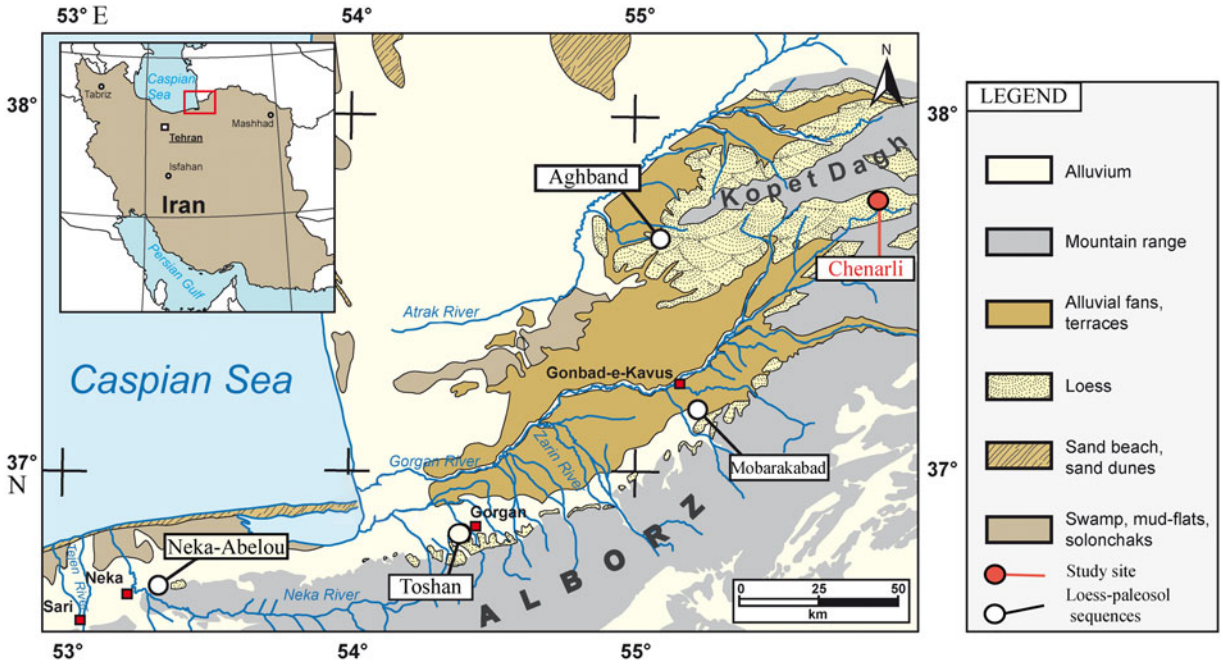

Figure 1. Map of northeastern Iran with locations of loess–paleosol sequences mentioned in the text, the distribution of loess deposits, and other geomorphological features (after Kehl et al., 2021). The loess–paleosol sequences of Neka-Abelou, Toshan, and Mobarakabad are situated along the northern footslopes of the Alborz Mountain range (NFAM), while the loess–paleosol sequences at Aghband and Chenarli are located in the northern Iranian Loess Plateau (NILP).

paleosols are generally magnetically enhanced, and suggest a relationship between increased fine-grained ferrimagnetic mineral content of surface soils with higher rainfall (e.g., Karimi et al., 2013; Ghafarpour et al., 2016; Najafi et al., 2019; Sharifigarmdareh et al., 2020; Kehl et al., 2021). These studies mainly focused on the alternating magnetic properties between loess and paleosols with little emphasis on the magnetic enhancement/dissolution mechanism.

We present here the first investigations of loess–paleosol sequences in the eastern NILP focusing on magnetic and colorimetric properties of the Chenarli sequence. Our aim is to characterize iron (hydr)oxide formation by measuring a suite of color and magnetic parameters. This information will help us to understand the magnetic enhancement/dissolution process in the modern soil and paleosols of the studied section. We further report the first luminescence and radiocarbon data for this sequence to provide a preliminary chronologic frame, with the goal of using these ages to link paleosols and modern soil formation in terms of (paleo)climate. Finally, we present a tentative regional stratigraphic correlation between the Chenarli section and other known loess–paleosol sequences in northern Iran to provide new insights into the regional timing of loess depositional phases and periods of pedogenesis.

GEOGRAPHIC AND CLIMATOLOGIC CONTEXT

Loess deposits in the NILP are found to have >60 m thickness (Lauer et al., 2017b). The oldest strata probably reach the Lower Pleistocene (Wang et al., 2016). Previous luminescence studies provide a geochronologic framework for loess–paleosol sequences and sand dunes in the wider study area of northern Iran (Frechen et al., 2009; Lauer et al., 2017a, 2017b; Rahimzadeh et al., 2019). These studies indicate that loess–paleosol sequences in this area span the interval from Marine Isotope Stage (MIS) 7 to MIS 1 (~220 to ~9 ka), whereas the sand dunes mainly accumulated in the Early Holocene (10–8 ka). The section at Chenarli (37°42′55.50″N, 55°49′13.10″E) is located in the southern Kopet Dagh fold belt and in the easternmost NILP (Fig. 1), at 490 m above sea level (m asl). A mean annual precipitation (MAP) of ~450 mm and a mean annual air temperature of 17°C characterize the currently semiarid climate. A typic xeric soil moisture regime is dominant in the area, and soil moisture is high from October to March and then drops sharply in summer, while average monthly air temperature reaches its peak of 28°C in July–August (Khormali et al., 2020).

MATERIAL AND METHODS

Spectrophotometric analysis

The sequence was sampled at 4 cm stratigraphic resolution, which resulted in a total of 826 samples for spectrophotometric analyses. Determination of the colorimetric properties was conducted by measuring the diffuse reflected light for the <2 mm fraction from all samples, using a Konica Minolta CM-5 spectrophotometer. The measurements followed a standardized procedure (2° standard observer and illuminant C) according to Eckmeier et al. (2013). The spectrophotometric analysis covers the visible light range from 360 to 740 nm in 10 nm increments. The obtained spectral information was converted to the Commission Internationale de l'Eclairage (CIE) using the SpectraMagic NX software (Konica Minolta). Color planes are defined in the CIE ($L^*a^*b^*$) system by the Cartesian axes a^* and b^*, which coincide at the achromaticity point. The a^* axis extends to the complementary colors red ($+a^*$) and green ($-a^*$), and the b^* axis extends to the complementary colors yellow ($+b^*$) and blue ($-b^*$). A third axis normal to a^* and b^* defines the lightness, L^*(Scheinost and Schwertmann, 1999).

https://doi.org/10.1017/qua.2023.5 Published online by Cambridge University Press

Reflectance data were processed to obtain percent reflectance in standard color bands (Judd and Wyszecki, 1975), that is, violet = 400–450 nm, blue = 450–490 nm, green = 490–560 nm, yellow = 560–590 nm, orange = 590–630 nm, and red = 630–700 nm. Percent reflectance in these color bands was calculated by dividing the percentage of reflectance in a color band by the total reflectance in a sample. First-derivative values of the color spectrum, expressed as percent per nanometer and plotted at the midpoint of the 10 nm calculation interval, are more amenable to interpretation than the untransformed reflectance spectra. Peak heights in first-derivative curves can represent a variety of minerals, specifically iron oxides (Deaton and Balsam, 1991). Hematite has a peak at 565–575 nm, and goethite has two first-derivative peaks, one at 525–535 nm and the other at 435 nm (Deaton and Balsam, 1991). The hematite and goethite concentrations in the studied samples are calculated from peak heights centered at 565 and 435 nm for hematite and goethite, respectively.

Magnetic analyses

Low-frequency susceptibility (χ_{lf}) and frequency-dependent susceptibility (χ_{fd}%) of all 826 samples were determined from measurements at frequencies of 505 and 5050 Hz in a 400 A/m field using a Magnon VFSM susceptibility bridge. The χ_{fd}% is expressed as χ_{fd} (%) = $[(\chi_{lf} - \chi_{hf})/\chi_{lf}] \times 100$, where χ_{lf} is the low-field magnetic susceptibility and χ_{hf} is the high-field magnetic susceptibility. In addition, 22 samples were selected from modern soil, paleosols, and loessic C horizons (hereafter LCH), which correspond to the highest and lowest χ_{lf} values of each loess unit, respectively, for isothermal remanent magnetization (IRM), susceptibility of anhysteretic remanent magnetization (χ_{ARM}), and temperature-dependent low-field susceptibility (χ-T) measurements.

The ARM imparted in a peak alternating field of 100 mT with a superimposed static bias field of 100 μT is magnetic concentration dependent and also grain-size dependent and particularly sensitive to grains with stable single domain (SD) behavior. ARM was induced using a Magnon AFD 300 demagnetizer, and χ_{ARM} was calculated by dividing mass-normalized ARM values by the bias field applied during ARM acquisition. The IRM was acquired stepwise from 0 to 2.75 T, backfield IRMs were then imparted stepwise from 0 to 300 mT, employing a Magnon PM II pulse magnetizer and 2-G Enterprises Model 760 cryogenic magnetometer for measurements. The "saturation" IRM (SIRM) is here defined as the IRM value measured at the 2.75 T step, even though samples were not completely saturated.

The χ-T measurements were carried out using a MFK1-FA Kappabridge system in combination with an AGICO CS3 furnace (Advanced Geoscience Instruments, Brno, Czech Republic) in the 20–700°C temperature range in an argon atmosphere to minimize oxidation. Results of temperature experiments were interpreted and evaluated using the software package CUREVAL (Hrouda, 1994). The magnetic parameters, methods, and magnetic interpretation used in this study are listed in Table 1. All magnetic measurements were made at the Grubenhagen rock magnetic laboratory of the Leibniz Institute for Applied Geophysics (LIAG) in Hanover, Germany.

Granulometric analysis

Particle-size distributions were determined for the same samples analyzed for ARM, IRM, and χ-T measurements by means of laser diffractometry using a Beckman-Coulter LS 13320 PIDS (Beuselinck et al., 1998; Machalett et al., 2008). We followed the standard sample protocol of Machalett et al. (2008), using the Fraunhofer theory for evaluating grain-size spectra without removing organic matter and carbonates from samples before the particle-size measurements. The samples were pretreated for at least 12 h in overhead tube rotators in a 1% ammonium hydroxide solution for particle disaggregation and dispersion before analysis. This method yields lower clay content than the pipette analyses, owing to a different measuring principle (Beuselinck et al., 1998). We therefore chose the sum of particles with sizes <5.5 μm in diameter to estimate the clay percentage. The 5.5 μm diameter was also applied to the grain-size data set of the Toshan loess–paleosol section (Vlaminck et al., 2016, 2018) in the NFAM for comparison with our results.

Radiocarbon dating

One radiocarbon age was determined using charcoal pieces from the Cky2 horizon (~10.3 m) of loess unit (LU) 2. Pretreatment involved standard acid–alkali–acid extraction; isotope measurements were conducted in the Cologne accelerator mass spectrometry lab facilities, Germany (for full preparation method, see Rethemeyer et al. [2013]). Conventional radiocarbon ages were calibrated using OxCal v. 4.3.2 (Ramsey, 2017) and the IntCal13 calibration curve (Reimer et al., 2013). Calibrated ages are reported as age ranges at the 2-sigma confidence level (95.4%).

Luminescence dating

Luminescence dating was applied to seven samples (Table 2) from the Bw horizon of LU 1 (0.4 m), the Cy horizon of LU 1 (1.8 m), the Cy1 horizon of LU 2 (4.2 m), the Cky2 horizon of LU 2 (8.5 and 10.5 m), the Ckyz horizon of LU 4 (21.5 m), and the C1 horizon of LU 7 (28.3 m). All measurements were conducted in the luminescence laboratory at LIAG, Hanover, Germany. The luminescence samples were collected from the LCH using light-tight plastic and steel tubes. Further material was taken from the surrounding sediment for gamma spectrometry to determine uranium, thorium, and potassium (^{40}K) concentrations. Nuclide concentrations were measured with a high-purity germanium type-N detector. The average dose rate of the loess units is 3.4 Gy/ka, values range from 3.34 ± 0.22 Gy/ka to 3.54 ± 0.22 Gy/ka. Dose-recovery tests were conducted. Six aliquots of each sample were bleached under a solar lamp for 5 h. After the signal was reset, the remaining dose was measured for three aliquots using the $pIRIR_{225}$ protocol. For the other three aliquots, a well-known dose close to the expected natural dose was given. This dose was then treated as unknown, and we then tried to recover this dose. Anomalous fading was also measured after irradiating a similar dose to the equivalent dose (De) for each sample using three to four aliquots per sample. The De value, dose-recovery ratio, and fading rate were calculated for $pIRIR_{225}$ signals. The mean measured dose residual value was then subtracted from the recovered doses, the ratio of (subtracted) measured dose/given dose was used as a quality check for the $pIRIR_{225}$ protocol (Kehl et al., 2021), and g-values were determined following the procedure of Huntley and Lamothe (2001).

RESULTS AND DISCUSSION

Stratigraphy and age control of the Chenarli profile

The Chenarli section is a 34-m-thick loess–paleosol sequence exposed in a stepped profile of an artificial trench dug down to

https://doi.org/10.1017/qua.2023.5 Published online by Cambridge University Press

Table 1. Magnetic parameters used in this study.

Name	Method	Magnetic interpretation
Low-frequency magnetic susceptibility (χ_{lf})	Measured using a Magnon VFSM susceptibility bridge. Units: m^3/kg.	χ_{lf} is a proxy for the abundance of all ferrimagnetic magnetic minerals (Geiss, 2014).
Frequency-dependent susceptibility (χ_{fd})	Determined from measurements at frequencies of 505 and 5050 Hz and at a field of 400 A/m using a Magnon VFSM susceptibility bridge. The frequency dependence is expressed as $\chi_{fd}\ \% = [(\chi_{lf} - \chi_{hf})/\chi_{lf}] \times 100$.	χ_{fd} is a proxy for ultrafine ($d < 0.01$ μm) magnetic particles (Dearing et al., 1996; Worm, 1998).
Curie temperature measurement (χ_T)	Performed using an AGICO CS3 furnace apparatus in the 20–700°C temperature range in an argon atmosphere. The CS3 furnace works in combination with the AGICO MFK1-FA Kappabridge. Results were interpreted and evaluated using the CUREVAL software (Hrouda, 1994).	A distinct loss of susceptibility is observed at about ~585° C, which suggests a ferrimagnetic component close to magnetite as the principal magnetic mineral. The susceptibility loss at ~300–450°C is caused by the conversion of ferrimagnetic maghemite to weakly magnetic hematite (Oches and Banerjee, 1996; Deng et al., 2001).
Anhysteretic remanent magnetization (ARM)	Acquired in an alternating field (AF) of 100 mT with a superimposed 100 μT bias field using a Magnon AFD 300 demagnetizer. Units: Am^2/kg.	Provides an estimate of the presence of small (0.05–0.06 μm) single-domain grains; sensitive to both the concentration and grain size of ferrimagnetic minerals (Quinton et al., 2012).
χ_{ARM}	Anhysteretic susceptibility, which is the ARM divided by the DC bias field. Units: m^3/kg.	Interpretation: same as ARM
Isothermal remanent magnetization (IRM) and backfield IRM	Acquired stepwise from 0 to 2.75 T and backfield IRM stepwise from 0 to 300 mT, employing a Magnon PM II pulse magnetizer and using 2-G Enterprises Model 760 cryogenic magnetometer for measurements. Units: Am^2/kg.	Estimates the abundance of all remanence-carrying ferrimagnetic (magnetite and maghemite) minerals; depends strongly on the presence of large ($d > 1$–2 μm) ferrimagnetic particles, which have likely been inherited from the parent material (Geiss, 2014).
Saturation isothermal remanent magnetization (SIRM)	Defined as the IRM value measured after the 2.75 T step, even though samples were not completely saturated. Units: Am^2/kg.	Indicates the presence and abundance of all remanence-carrying ferrimagnetic and antiferromagnetic (hematite) particles (Evans and Heller, 2003).
"Hard" IRM (HIRM)	$HIRM_{300} = 0.5 \times (SIRM + IRM_{-300mT})$. Units: Am^2/kg.	Reflects the magnetic signals carried by the weakly magnetic, high-coercivity antiferromagnetic minerals, such as hematite and goethite (Robinson, 1986; Thompson and Oldfield, 1986).
S-ratio	$0.5 \times (SIRM - IRM_{-300mT})/SIRM$ (Bloemendal et al., 1992).	Provides a relative measure of the contributions of low- and high-coercivity material to SIRM of a sample (Heslop, 2009). Values between 1 and 0.5 indicate greater than 50% remanence held by a soft component, and values less than 0.5 indicate greater than 50% remanence held by a hard component. A value of 0.5 indicates remanence held equally by soft and hard minerals (Maxbauer et al., 2016).

in situ loess deposits along a steeply inclined northwest-facing slope (Fig. 2A). The section contains eight loess units separated by paleosols (see Fig. 3 for stratigraphy). The loess units at Chenarli are correlated tentatively to Marine Isotope Stages (Martinson et al., 1987), and are ordered from oldest (LU 8) to youngest (LU 1) (Fig. 3). The eight loess units at Chenarli are defined based on the International Stratigraphic Guide (Salvador, 1994), in which loesses are stratigraphic units but soils and paleosols are not. Soils and paleosols developed within predeposited loess stratigraphic units and mark the boundaries between loess stratigraphic units.

The loess record at Chenarli extends from >130 ± 9.1 ka to the Early Holocene. The uppermost LU 1 yielded a luminescence age of 9.8 ka ± 0.7 (CHE-3858; Table 2) and hosts the modern soil that formed under steppe-like vegetation. The modern soil is a 2-m-thick, A-Bw-Bk-Cy profile and is classified as a haploxerept in the USDA soil taxonomic system (Soil Survey Staff, 2014). We note that the degree of modern soil development was surprising to us in view of the absence of calcic horizons, which modern soils typically have in the study area (Sharifigarmdareh et al., 2020). Calcic horizons in the modern soil may be lacking because of episodic erosion in the relatively unstable loess hillslopes. Feldspar grains yielded an age of 13.01 ± 0.9 ka for the Cy horizon of LU 1 (Table 2). Hence, loess deposition in LU 1 has intensified, probably coinciding with the onset of the Younger Dryas event.

LU 2 (Fig. 2B) is ~9 m thick, and consists of largely pedogenically unaltered eolian deposits including calcium carbonate, gypsum, and soluble salts (Fig. 3). The upper contact of LU 2 is demarcated by a weakly developed paleosol (Bwb). A luminescence sample from 20 cm below this paleosol, 4.2 m below the surface, produced an age estimate of 16.5 ± 1.5 ka (Table 2). Therefore, this weakly developed paleosol in LU 2 probably formed during the Bølling-Allerød interstadial and may have been coeval with the last transgression of the Caspian Sea (Khvalynian highstand), beginning at ~16 ka (Chepalyga, 2007). Some mollusk shells and centimeter-scale charcoal pieces are present 9–10.5 m below the surface (Fig. 3). A 4.5-m-thick loess accumulation (Cy1 and Cky1 horizons) in LU 2 appears coeval with the last glacial maximum (LGM; defined as the period ~26–19 ka in Clark et al. [2009]). Feldspar grains from the Cky2 horizon of LU 2, at 8.5 and 10.5 m, returned luminescence ages of 28.2 ± 2.0 ka and 30.8 ± 2.5 ka, respectively (Fig. 3,

https://doi.org/10.1017/qua.2023.5 Published online by Cambridge University Press

Table 2. Gamma spectroscopy and luminescence dating results.[a]

Sample ID	Profile depth (m)	U (ppm)	Th (ppm)	K (%)	Cosmic DR (Gy/ka)	Total DR (Gy/ka)	De $pIRIR_{225}$ (Gy)	g-value $pIRIR_{225}$	$pIRIR_{225}$ age (ka); uncorr.	Corr. age (ka)[b]
CHE-3858	0.4	2.40 ± 0.12	8.92 ± 0.45	1.64 ± 0.08	0.07	3.46 ± 0.22	30.95 ± 0.22	0.95 ± 0.1	8.95 ± 0.6	9.8 ± 0.7
CHE-3859	1.8	2.42 ± 0.12	8.42 ± 0.42	1.61 ± 0.08	0.07	3.35 ± 0.21	40.00 ± 0.32	0.95 ± 0.1	11.96 ± 0.8	13.01 ± 0.9
CHE-3860	4.2	2.37 ± 0.12	8.54 ± 0.43	1.61 ± 0.08	0.07	3.29 ± 0.21	53.51 ± 0.48	0.15 ± 0.6	16.24 ± 1.6	16.5 ± 1.5
CHE-3861	8.5	2.30 ± 0.12	8.25 ± 0.41	1.56 ± 0.08	0.07	3.14 ± 0.21	78.68 ± 1.16	1.29 ± 0.2	25.06 ± 1.7	28.2 ± 2
CHE-3862	10.5	2.39 ± 0.12	8.37 ± 0.42	1.58 ± 0.08	0.07	3.21 ± 0.21	82.34 ± 1.19	1.94 ± 0.4	25.63 ± 1.7	30.8 ± 2.5
CHE-3866	21.5	2.54 ± 0.12	9.89 ± 0.50	1.77 ± 0.08	0.07	3.54 ± 0.22	270.23 ± 7.09	1.66 ± 0.1	76.27 ± 5.2	89.6 ± 6.4
CHE-3870	28.3	2.49 ± 0.12	8.97 ± 0.45	1.68 ± 0.08	0.07	3.34 ± 0.22	364.44 ± 7.11	1.74 ± 0.1	109.27 ± 7.4	130 ± 9.1

[a]Abbreviations: DR, dose rate; De, equivalent dose; (un)corr., (un)corrected.
[b]Huntley and Lamothe (2001).

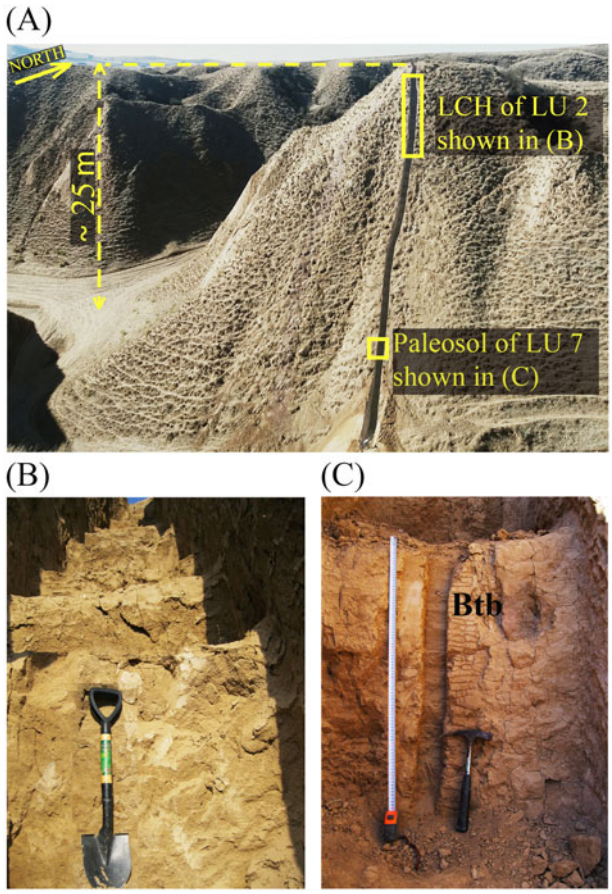

Figure 2. The studied section at Chenarli with yellow boxes indicating locations of the loessic C horizons (LCH) in loess unit (LU) 2 and paleosol of LU 7. Close-up view of (B) the LCH of LU 2 and (C) Btb horizon of LU7 in A. Photographs by A. Ghafarpour.

Table 2). These ages are consistent with a radiocarbon age of 29–28.4 cal ka BP (COL5898.1.1) obtained on a piece of charcoal found in this horizon at a depth of ~10.3 m (Fig. 3). Together, these ages from LU 2 point to a relatively long period of loess deposition spanning between ca. 30.8 ka and 16.5 ka. The Cy2 horizon occurs in the lower part of LU 2, which indicates ~2.5 m of loess accumulation before 30.8 ± 2.5 ka. (Fig. 3).

LU 3 ranges from ~13 to 17.5 m below the surface. At the top of this unit, a 5- to 7-cm-thick weak Ab horizon is present. The upper 2 m of LU 3 represents a pedogenically altered, dark-brown soil with secondary gypsum and calcium carbonate (Bkyb and BCkyb horizons). Small mollusk shells are present in the paleosol and Cky horizon of LU 3 (Fig. 3). The underlying LU 4 comprises the Bkyb, Bkb, and Ckyz horizons, including carbonate nodules and mollusk shells. Soluble salts are present in the lower 1.7 m (Ckyz) of this unit. Luminescence dating from the Ckyz horizon of LU 4 yielded an age of 89.6 ± 6.4 ka (Table 2), which correlates well with MIS 5b, and therefore we infer that the paleosol of LU 4 probably formed during MIS 5a (Fig. 3).

The upper parts of LU 5 and LU 6 are pedogenically altered (Byb and Bkyb horizons), while the Cyz horizon of the LU 5 and Ckyz horizon of LU 6 reflect eolian depositional phases, and contain small mollusk shells (Fig. 3). The uppermost 1.8 m of LU 7 (Fig. 2C) is a well-developed paleosol (Btb horizon) that has visibly clear signs of clay lessivage and Fe mottles. The upper 0.7 m of this Btb horizon lies at a depth of ~26.2 m

https://doi.org/10.1017/qua.2023.5 Published online by Cambridge University Press

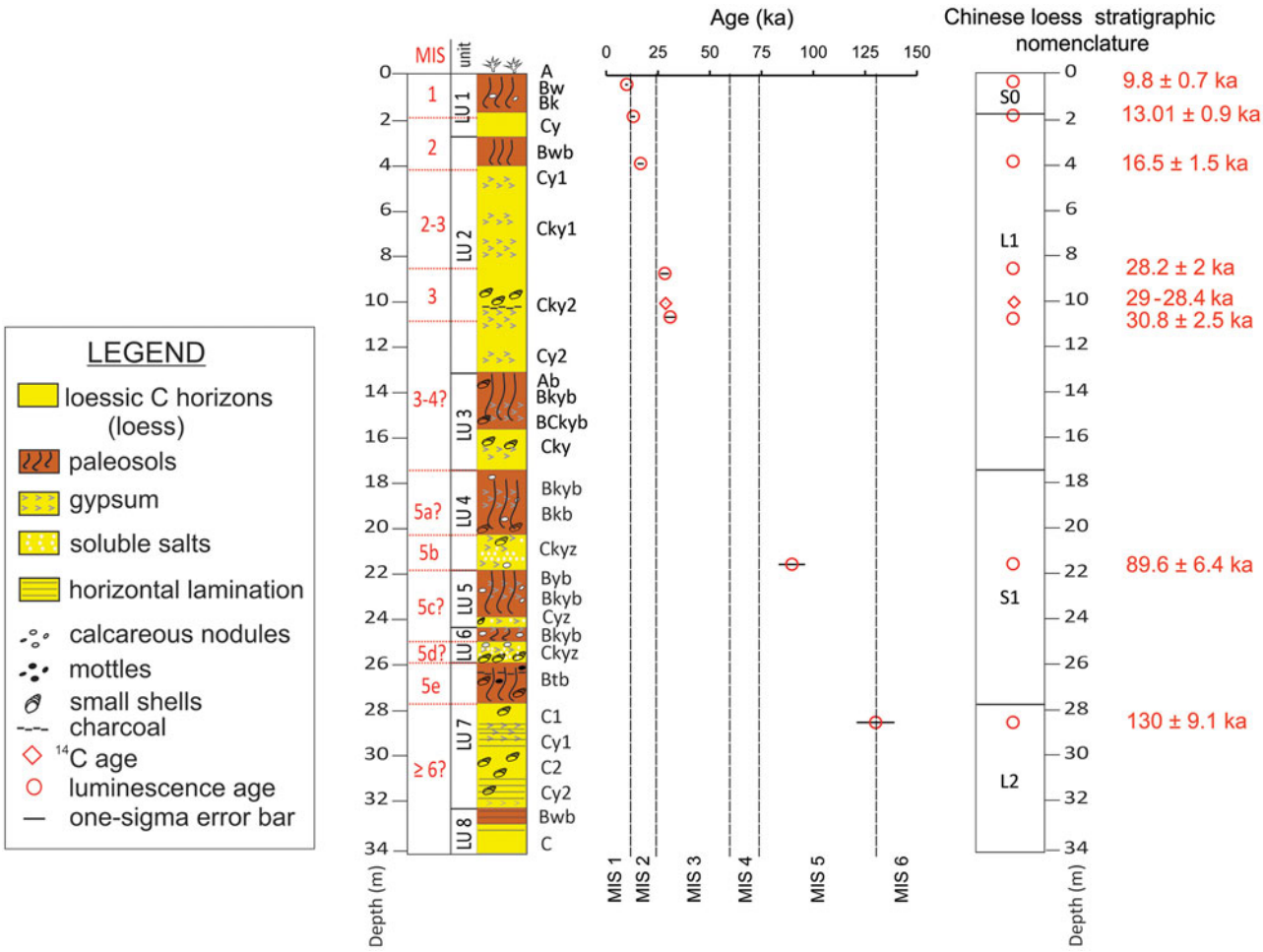

Figure 3. Stratigraphic section at Chenarli, with bedding characteristics, buried soils (paleosols) with recognized horizons, and radiocarbon and luminescence ages (see Table 2 for details). The sequence was divided into a suite of sedimentary units (see text). In the stratigraphic column, A, B, and C represent the master soil horizons within loess units (Soil Survey Staff, 2014). Lowercase letters are used as suffixes to designate specific subordinate distinctions within horizons. The suffix symbol meanings are as follows: b, buried genetic horizon; k, accumulation of secondary carbonates; t, accumulation of silicate clay; w, development of color or structure; y, accumulation of gypsum; z, accumulation of soluble salts (Soil Survey Staff, 2014). Marine Isotope Stage (MIS) ages are adopted from Martinson et al. (1987). A tentative comparison with Chinese loess stratigraphic nomenclature (Kukla and An, 1989) is also shown (right-hand side).

below the surface and contains pieces of charcoal and small mollusk shells. The age of the upper C1 horizon of LU 7, immediately below the Btb horizon, at a depth of about 28.3 m, is 130 ± 9.1 ka (Fig. 3, Table 2). Therefore, periods of pedogenesis between ca. 89.6 ± 6.4 and 130 ± 9.1 ka in LU 5-7 probably date to MIS 5c and 5e (Fig. 3). The basal ~4 m of this unit has millimeter-scale horizontal laminations. The lowermost LU 8 is moderately sorted with diffuse millimeter- to centimeter-scale horizontal laminations. The upper contact of LU 8 is demarcated by a weakly developed paleosol (Bwb; see Fig. 3).

In combination the stratigraphic record and luminescence ages provide a tentative chronologically constrained depositional record at Chenarli. Comparison with other loess–paleosol sequences in northern Iran (see Fig. 9 in "Periods of Loess Deposition and Pedogenesis from MIS 5d to the Holocene") sheds further light on the paleoclimatic history of the northern Iranian loess records.

Diachronic change in iron oxides and implications for magnetic susceptibility enhancement

L* values vary between 54.7 and 66.3, and maxima in L* values are observed in the LCH of the studied sequence, while the modern soil and paleosols have the lowest values (Fig. 4). Determination of soil color yields b* values of 10.74–15.33 (Fig. 4). The b* values have similar trends to the L* values, although b* values do not contrast strongly between paleosols and LCH, probably because of accumulation of carbonate, gypsum, and soluble salts in the paleosols. In marked contrast, a* values, which range from 3.34 to 6.64, are noticeably higher in the modern soil and paleosols than in LCH (Fig. 4). The DRS goethite peak at 435 nm correlates positively with L* values of the studied samples (Fig. 5A), while a* values have a positive correlation with the hematite peak at 565 nm (Fig. 5B).

The highest L* values (Fig. 4) and goethite content in the Cky2 horizon of LU 2 (Fig. 5C) suggest eolian goethite input during the period of loess accumulation dating to about late MIS 3–MIS 2. In contrast, the paleosols of LU 4-LU 7 have higher a* values (Fig. 4) and hematite concentration compared with those from other paleosols and modern soil (Fig. 5C). Therefore, greater pedogenic hematite formation in LU 4-LU 7 paleosols offers an analog of environmental response to more seasonal wet–dry cycles during MIS 5. Additionally, DRS results indicate a decline in goethite concentration in the modern soil and paleosols compared with LCH, while hematite formation is at its maximum in the modern

https://doi.org/10.1017/qua.2023.5 Published online by Cambridge University Press

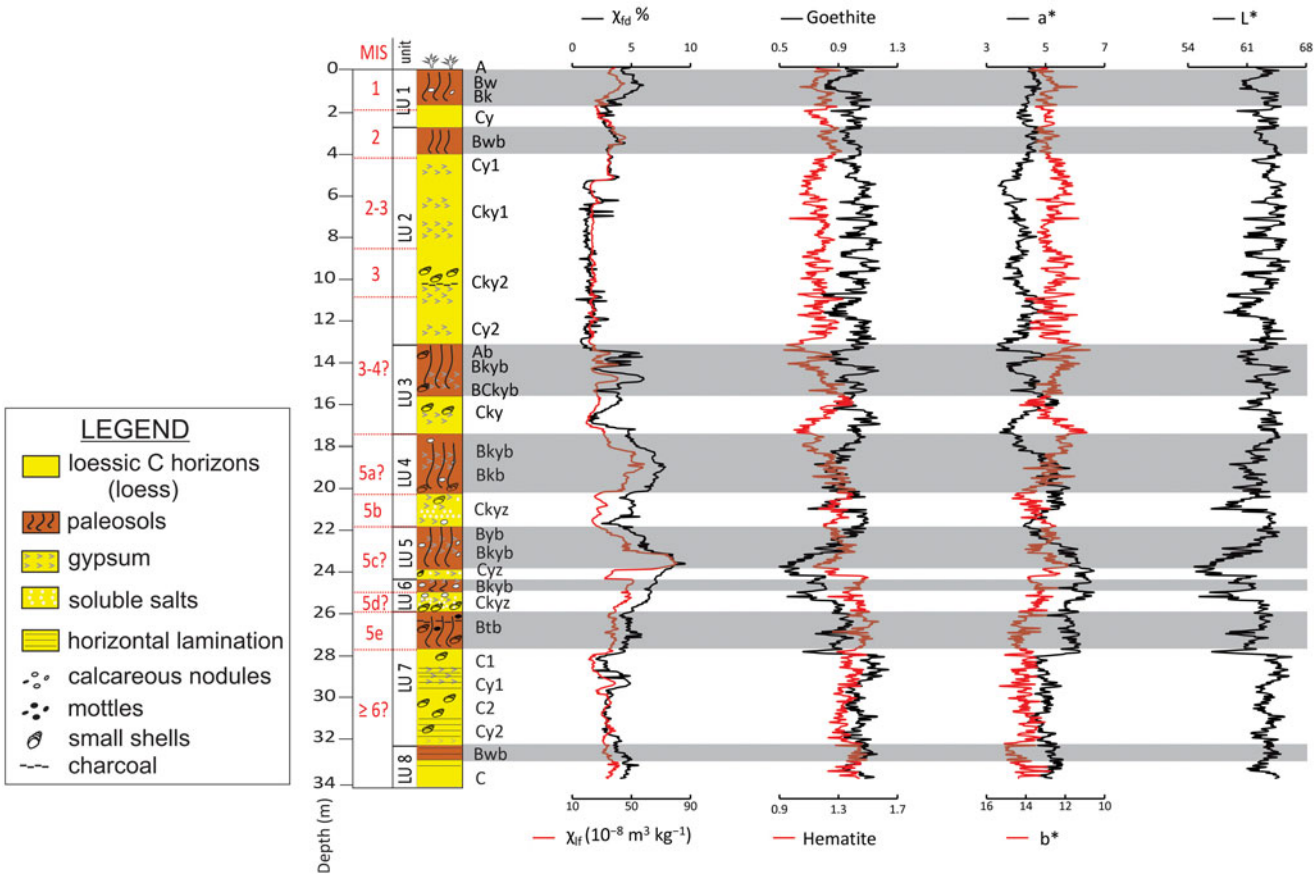

Figure 4. Stratigraphic variation of low-frequency susceptibility (χ_{lf}), frequency-dependent susceptibility (χ_{fd}%), goethite, hematite, a*, b*, and L*values. Gray bars mark the modern soil and paleosols within the loess units.

soil and paleosols (Fig. 4). Therefore, our DRS data suggest lower goethite formation and/or dehydroxylation compared with hematite during burial, but greater pedogenic hematite formation during pedogenesis, coupled with warmer and more seasonal climatic conditions (Jiang et al., 2022 and references therein). This finding is consistent with previous studies, which suggest that hematite formation reaches its maximum in Mediterranean and subtropical soils with extended dry seasons (Cornell and Schwertmann, 2003; Maxbauer et al., 2016). In addition, at least in part, hematite formation in the modern soil and paleosols may be the result of seasonal moisture in the study area that links pedogenic hematite formation with local MAP, potential evapotranspiration, and the soil moisture budget. We note that with our DRS data it is not possible to discriminate pedogenic hematite from eolian hematite input in the modern soil and paleosols. Hence, the possibility of eolian hematite must be considered when interpreting results for the paleosols.

Stratigraphic variations of χ_{lf} and χ_{fd}% are shown in Figure 4. χ_{lf} in LCH ranges between 19.4 and 31×10^{-8} m^3/kg and χ_{fd}% varies between 0.6% and 3.5%. The modern soil and paleosols have higher χ_{lf} and χ_{fd}% than LCH. In addition, positive correlation between χ_{lf} and χ_{fd}% ($R^2 = 0.78$; Fig. 6A) and elevated χ_{lf} and χ_{fd}% values point to an increased superparamagnetic (SP) fraction due to pedogenesis in paleosols. Higher a* values in the modern soil and paleosols compared with LCH are accompanied by high χ_{lf} and χ_{fd}% values (Fig. 4). However, in the Btb horizon of LU 7, χ_{lf} and χ_{fd}% are significantly reduced when a* values are high (Fig. 4). Therefore, compared with χ_{lf} and χ_{fd}%, the a* value might be a more reliable paleoclimatic indicator (Hu et al., 2014) in the loess–paleosol sequences of the NILP and NFAM (Ghafarpour et al., 2021a). We also ascribe the increased hematite content and χ_{fd}% values in the modern soil and paleosols (Fig. 4) to the fact that in well-developed soils and paleosols, magnetic enhancement is due to the transformation of weakly magnetic, Fe-rich phases into strongly ferrimagnetic particles and also hematite and goethite. Increased χ_{fd}% and hematite content were also observed in the modern soil and paleosols of the Mobarakabad section (Ghafarpour et al., 2021a). Therefore, we postulate that pedogenic magnetite/maghemite and hematite formation in the paleosols of NILP and NFAM was almost certainly governed by similar climatic conditions, with alternating wet–dry cycles (Maher et al., 2003; Orgeira et al., 2011), which are consistent with the current Mediterranean climate in the area. This implies that the local hydroclimate must be considered when interpreting soil hematite contents.

Magnetic enhancement/dissolution mechanisms in loess units

The χ-T curves of representative samples from Cky2 horizon of LU 2 and paleosols (Bkyb horizons of LU 4 and LU 5, and Btb horizon of LU 7) of the Chenarli section are shown in Figure 6B. They suggest the existence of hematite with Néel temperature of 675°C in both the LCH and paleosols. Noticeable humps at ~280–400°C in Bky(b) horizons of modern soil and

https://doi.org/10.1017/qua.2023.5 Published online by Cambridge University Press

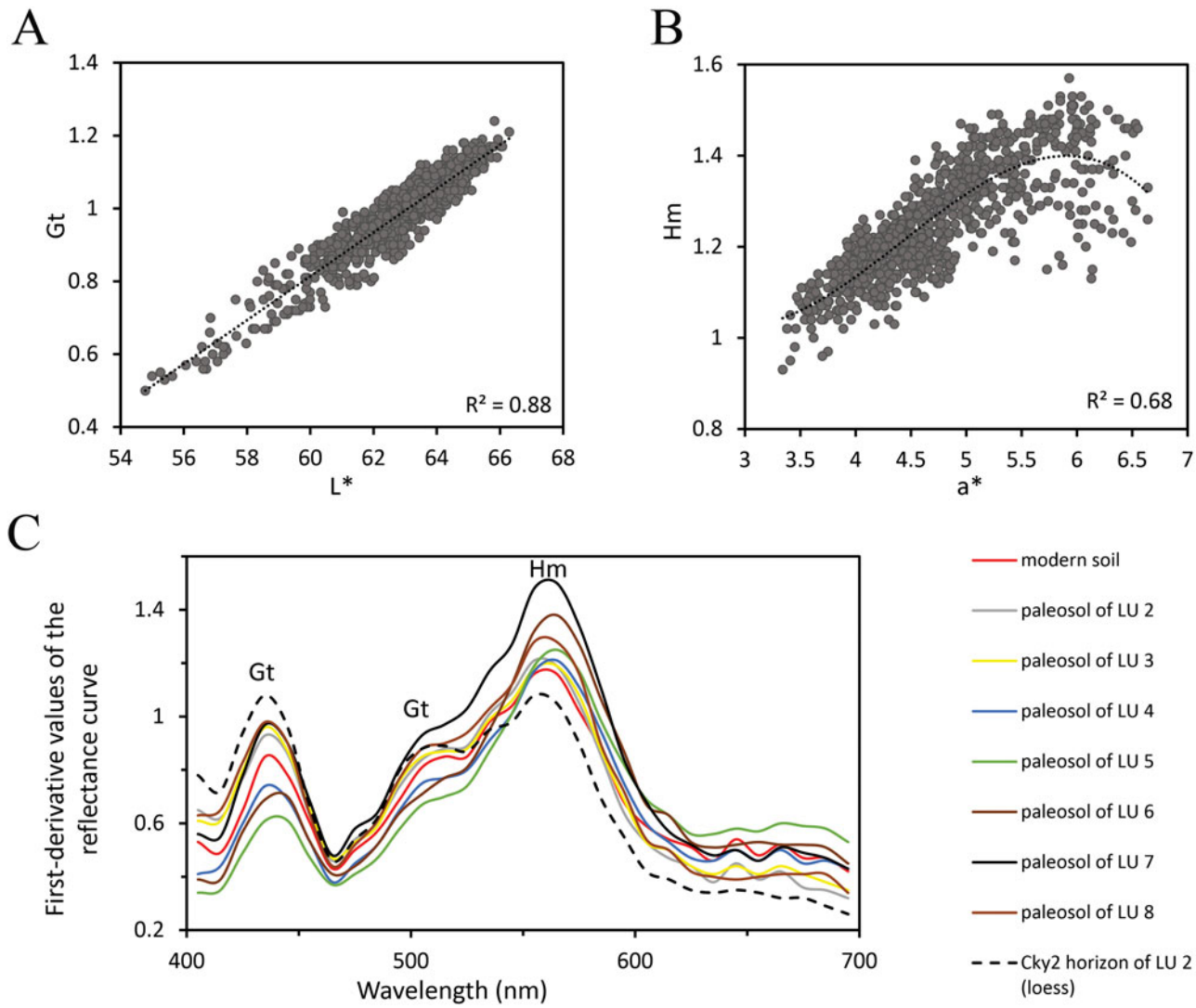

Figure 5. Scatter plots of (A) first-derivative values of the 435 nm goethite peak vs. L* values, (B) first-derivative values of the 565 nm hematite peak vs. a* values, (C) first-derivative values of the reflectance curve vs. wavelength for the Cky2 horizon of LU 2 (black dashed line) and selected paleosol samples from loess unit (LU) 1 to LU 8. The peaks indicate the presence of Fe (oxyhydr)oxides (Gt, goethite; Hm, hematite) in the samples. The highest first-derivative 565 nm peak height (Hm) is observed in the paleosol of LU 7, while the goethite peak at 435 nm is higher in the Cky2 horizon of LU 2 than in the paleosols (see text). When both hematite and goethite occur, the hematite peak at 565 nm overwhelms the 525–535 nm goethite peak, and goethite tends to increase the area under the hematite peak, causing the shoulder at 525–535 nm (Balsam and Damuth, 2000).

paleosols are caused by the conversion of ferrimagnetic maghemite to weakly magnetic hematite (Sun et al., 1995; Oches and Banerjee, 1996; Deng et al., 2001). However, the distinctly shallower slope of susceptibility loss at about 300°C in the Btb horizon of LU 7 may be due to a small amount of maghemite (Fig. 6B). A χ-T heating curve for the Cky2 horizon of LU 2 suggests an absence of pedogenic magnetite/maghemite (Fig. 6B).

χ_{ARM} (0.34 to 1.74×10^{-6} m^3/kg) and IRM (1.62 to 4.02×10^{-3} Am^2/kg) have higher values in paleosols than in LCH (Fig. 7). Variations of IRM at a backfield of 300 mT ($IRM_{-300\ mT}$) and SIRM of selected samples are summarized in Figure 7. The measured IRM acquisition curves undergo a major increase below 300 mT (Fig. 8A), which supports the interpretation of a dominant contribution from magnetite and maghemite. The slight increase between 300 and 2500 mT is consistent with the presence of hematite (Fig. 8A). ARM generally represents fine SD grains (Geiss, et al., 2008), and therefore the increase in χ_{fd}% and χ_{ARM} values in the paleosols (Fig. 7) indicates that the magnetically enhanced horizons contain mixtures of (ultra)fine ferrimagnetic particles and SD grains. The magnetic grain size–dependent ratio χ_{ARM}/IRM of samples ranges from 2.06×10^{-4} m/A in LCH to 7.67×10^{-4} m/A in the modern soil and paleosols (Fig. 7). Also, a strong correlation ($R^2 = 0.93$) exists between χ_{ARM}/IRM and χ_{fd}%, with the exception of samples from the Btb horizon of LU 7 (Fig. 8B). χ_{ARM}/IRM is used to estimate the relative abundance of small and stable SD particles (Geiss and Zanner, 2006). The magnetic grain-size distribution of the LCH is characterized by the lowest percentage of fine SP and SD particles and highest fraction of coarse-grained particles, as indicated by minima in χ_{fd}% and χ_{ARM}/IRM (Fig. 7). Therefore, higher χ_{ARM}/IRM values and χ_{fd}% in the modern soil and paleosols than in LCH (Fig. 8B) suggest that *in situ* production of such magnetic particles causes magnetic enhancement of the modern soil and paleosols. In addition, strong correlation between

https://doi.org/10.1017/qua.2023.5 Published online by Cambridge University Press

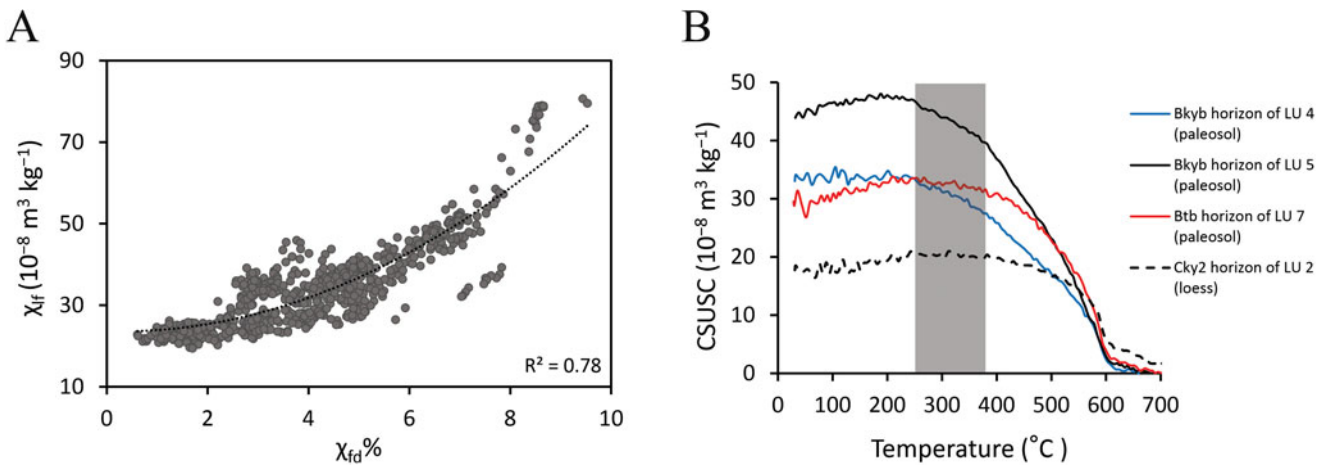

Figure 6. (A) χ_{lf} vs. χ_{fd}% of the studied samples and (B) the magnetic susceptibility (CSUS) heating curves from the Cky2 horizon of loess unit (LU) 2, the Bkyb horizons of LU 4 and LU 5, and the Btb horizon of LU 7 at Chenarli. The gray bar highlights a gradual susceptibility decrease starting from ~280–400°C during heating of the buried horizon samples in LU 4, LU 5, and LU 7, which indicates the conversion of ferrimagnetic maghemite to weakly magnetic hematite, even though the shallower slope of susceptibility loss at ~300°C in the Btb horizon of LU 7 could be due to only a smaller amount of maghemite. The χ-T curves of samples from the Cky2 horizon of LU 2 suggest the absence of pedogenic magnetite/maghemite (see text).

χ_{ARM}/IRM and χ_{fd}% (Fig. 8B) suggests a single consistent magnetic enhancement mechanism in the modern soil and paleosols, that is, addition of fine magnetic particles. However, samples from the Btb horizon of LU 7 follow a different pattern (red in Fig. 8B).

The granulometric properties indicate clay (<5.5 µm) proportions between 24.2% and 55.9%, with higher values in the modern soil and paleosols than in LCH (Fig. 7). The well-developed Btb horizon of LU 7 has the highest clay content (~38% to 56%). High χ_{ARM}/IRM values combined with a large clay fraction in the modern soil and paleosols (Fig. 7) indicate that finer SD ferrimagnetic particles are relatively concentrated in clay fractions, which is associated mostly with pedogenesis. Accordingly, high χ_{ARM}/IRM but low values of χ_{fd}% and χ_{lf} in the Btb horizon of LU 7 indicate a dominance of SD particles over SP particles, possibly because of the grain size–dependent vertical migration of smaller SP grains downward and to washing out of SP grains from this horizon. This would require high χ_{fd}% values below this horizon, which is not the case. In addition, it is unlikely

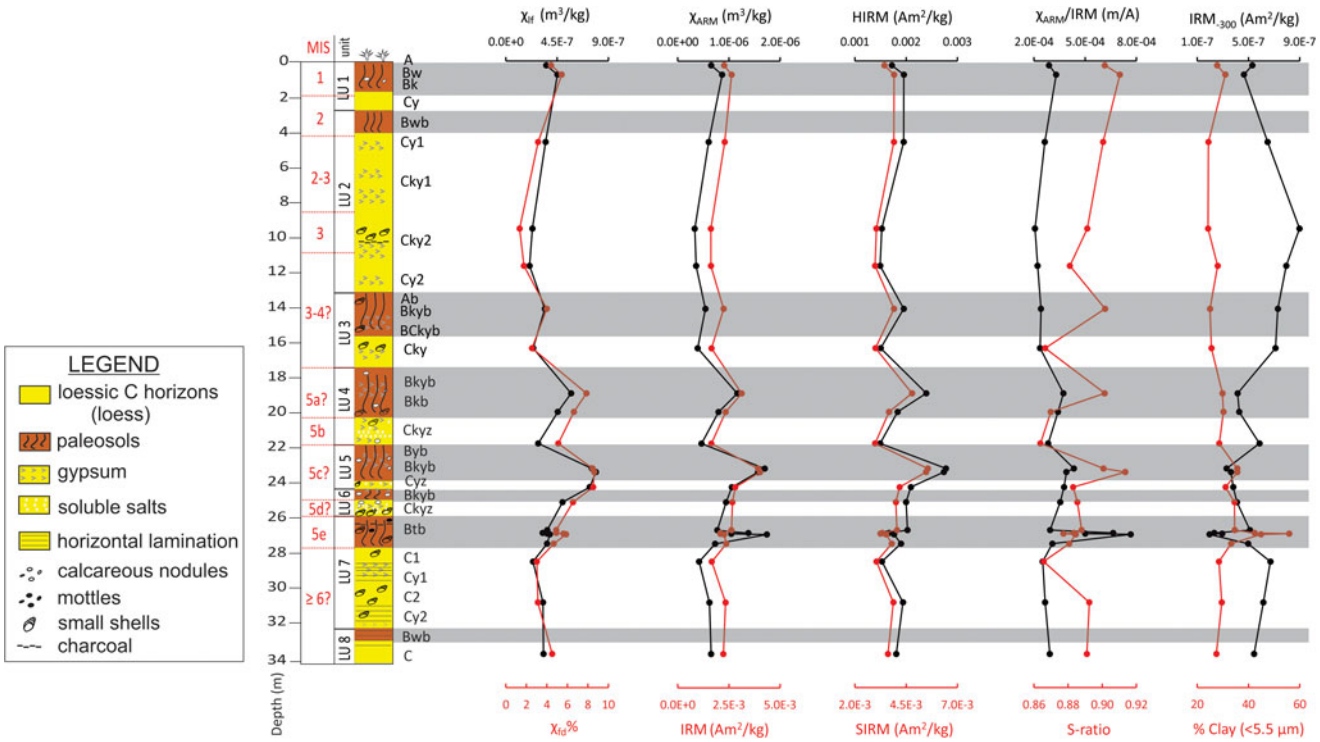

Figure 7. Stratigraphic column with magnetic properties and clay content of modern soil loessic C horizons (LCH) and paleosol samples in the Chenarli section. Gray bars mark the modern soil and paleosols within the loess units. χ_{ARM}, susceptibility of anhysteretic remanent magnetization; IRM, isothermal remanent magnetization; SIRM, "saturation" IRM; HIRM, "hard" IRM.

https://doi.org/10.1017/qua.2023.5 Published online by Cambridge University Press

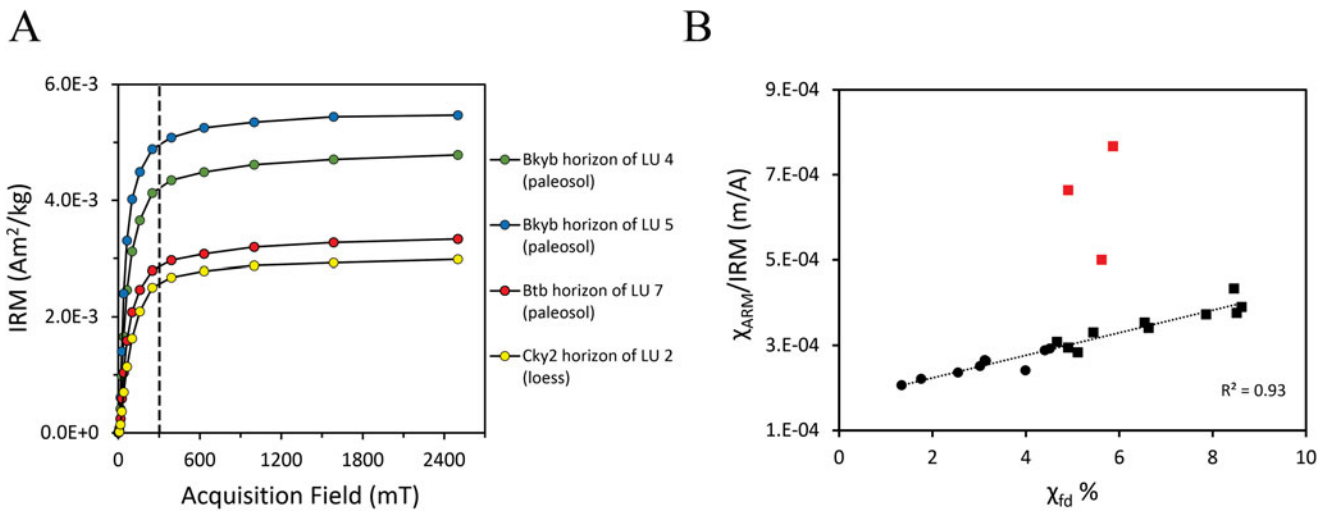

Figure 8. (A) Isothermal remanent magnetization (IRM) acquisition curves for selected samples from Chenarli (same samples as in Fig. 6B). The dashed vertical line at 300 mT is shown to aid distinction between low- and high-coercivity portions of the IRM acquisition curves. (B) The ratio of the susceptibility of anhysteretic remanent magnetization (χ_{ARM}) to IRM vs. χ_{fd}% of the studied samples. With increasing pedogenesis from loessic C horizons (black circles) to paleosols (black squares), both χ_{fd}% and χ_{ARM}/IRM increase. Higher χ_{ARM}/IRM values indicate a greater abundance of single-domain magnetic particles and higher χ_{fd}% suggests an increase in ultrafine magnetic particles. There is a noticeable anomaly in the samples from the Btb horizon of LU 7 (red squares).

that the increased SD magnetite fraction resulted from an increased detrital input, because the high clay content in the Btb horizon of LU 7 does not suggest coarser sediments and increased detrital input.

Another explanation for low χ_{lf} and χ_{fd}% values in the Btb horizons of LU 7, which probably formed during MIS 5e, could be high amounts of paramagnetic clays (Geiss and Zanner, 2007). However, previous studies indicate that in the loessic

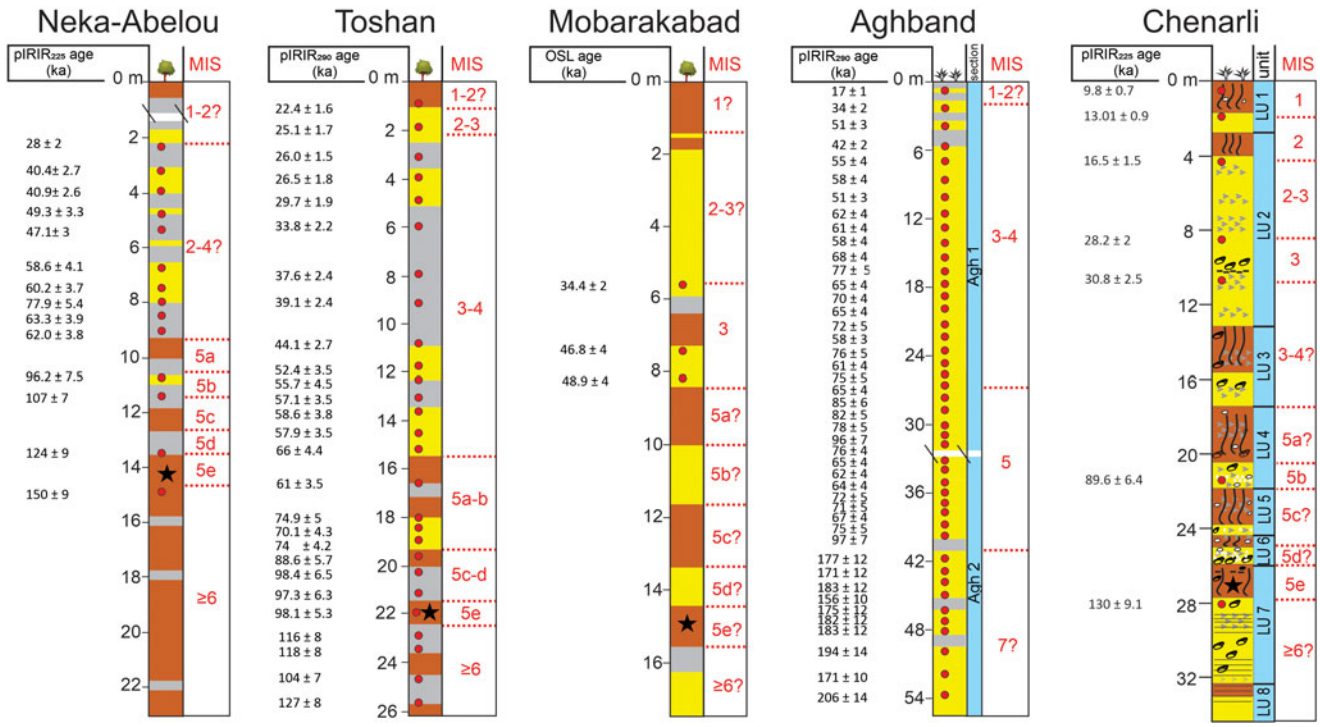

Figure 9. Comparison between the stratigraphy of the Chenarli section with simplified stratigraphic sections of loess–paleosol sequences at Neka-Abelou (36° 38′43″N, 53°19′15″E, 105 m asl), Toshan (36°49′01″N, 54°25′25″E, 145 m asl), Mobarakabad (37°09′32″N, 55°18′14″E, 310 m asl), and Aghband (37°37′06″N, E 55° 09′27″, 183 m asl) in northern Iran (for locations of sections, see Fig. 1). Loess horizons in the simplified stratigraphic sections of Neka-Abelou, Toshan, Mobarakabad, and Aghband are shown in yellow, weakly developed paleosols (Bwb, BCb, CBb, horizons) in gray, and well-developed paleosols (Bkb, Btb, Btkb, and Btgb horizons) in brown. See Fig. 3 for bedding characteristics and symbol legend of the Chenarli section. Marine Isotope Stage (MIS) ages are adopted from Martinson et al. (1987). Stars indicate paleosols that probably formed during MIS 5e in which magnetic depletion occurred. Source data are from Kehl et al. (2021) for Neka-Abelou, Vlaminck et al. (2018) for Toshan, Ghafarpour et al. (2017) for Mobarakabad, and Lauer et al. (2017b) for Aghband.

https://doi.org/10.1017/qua.2023.5 Published online by Cambridge University Press

modern soils of northern Iran, increasing clay content corresponds to both χ_{lf} and χ_{fd}% increases, although clays are weakly magnetic (Pourmasoumi et al., 2019; Sharifigarmdareh et al., 2020). In addition, high χ_{lf} and χ_{fd}% values are observed in the Btb horizons of loess–paleosol sequences of northern Iran (Ghafarpour et al., 2016; Vlaminck et al., 2018). This apparent contradiction may be because chlorite represents one of the dominant detrital clay minerals in the LCH of northern Iran (Khormali and Kehl, 2011; Ghafarpour et al., 2016). It is susceptible to weathering and provides free Fe for secondary ferrimagnetic mineral formation (e.g., Spassov et al., 2003; Torrent et al., 2007; Peng et al., 2014). Therefore, magnetic mineral concentration through lessivage, removal of carbonates (Singer et al., 1996), and chlorite weathering (He et al., 2018; Hyodo et al., 2020; Ye et al., 2020) are likely in these Bt(b) horizons. This might explain why high χ_{lf} and χ_{fd}% are observed in the Bt(b) horizons of loess–paleosol sequences in northern Iran. A more likely explanation for the high χ_{ARM}/IRM ratio but low χ_{fd}% and χ_{lf} values in the Btb horizon of LU 7, and the one that is preferred here, is the selective dissolution of SP particles in preference to SD under anoxic conditions (see "Last Interglacial (MIS 5e)").

Grain-size dependence of hematite proxies in the modern soil and paleosols

The "hard" IRM (HIRM) ranges between 1.49 and 2.78×10^{-3} Am^2/kg and increases systemically with increasing pedogenesis in the modern soil and paleosols (Fig. 7). The S-ratio varies between 0.86 and 0.91, with higher values in the modern soil and paleosols than in the LCH (Fig. 7). Elevated HIRM values and S-ratios in the modern soil and paleosols compared to the LCH indicate an increase in the total high-coercivity mineral content, coincident with a relative increase in low-coercivity minerals (Fig. 7). Also, DRS data suggest higher hematite content in the modern soil and paleosols compared with the LCH (Figs. 4 and 5C). Therefore, increasing HIRM values in the modern soil and paleosols are interpreted to represent higher contributions of hard hematite to remanence and/or relatively rapid oxidation of pedogenic magnetite and maghemite to hematite (and possibly goethite). Lower S-ratio values in the LCH of LU 3-7 compared with LCH of LU 2 (Fig. 7) suggest the additional presence of high-coercivity minerals such as hematite or goethite during MIS 2–MIS 3 loess accumulation in LU 2. High S-ratio values (>0.88) in the modern soil and paleosols compared with LCH indicate that the pedogenically produced magnetic signal is caused predominantly by magnetite or maghemite.

Quinton et al. (2012) suggested that S-ratio changes represent relative changes in hematite abundance, while HIRM changes might also be indicative of shifts in coercivity of other minerals (Liu et al., 2007). The S-ratio will underestimate the relative hematite fraction and HIRM will underestimate the absolute hematite concentration (Roberts et al., 2020). In the paleosol (Btb horizon) of LU 7, both HIRM and S-ratio are low, in contrast to the modern soil and other paleosols (Fig. 7). In addition, DRS has the highest hematite peak at 565 nm in the paleosol of LU 7 compared to the modern soil and other paleosols (Fig. 5C). However, the low HIRM in the Btb horizon of LU 7 suggests that the magnetization in this paleosol is not considerably impacted by hematite or goethite. Hence, the most plausible explanation for the low S-ratio and HIRM values but high hematite peak at 565 nm in this paleosol is that very fine-grained SP hematite is undetected by HIRM because these grains do not hold a stable remanence. However, SP hematite contributes to the DRS signal. It is also possible that strong weathering coupled with short-term reducing conditions during MIS 5e favored SP particle depletion (reflected in low χ_{fd}% values), and promoted transformation of SD magnetite/maghemite particles to (SP) hematite (low S-ratio) in the Btb horizon of LU 7, although eolian input of (SP) hematite to the paleosol is possible. Therefore, low HIRM values in the well-developed paleosol of LU 7 compared with the modern soil and other paleosols suggest that HIRM cannot be used alone as a proxy for the absolute concentration of magnetically hard minerals if their coercivity values are unknown (Liu et al., 2007; Quinton et al., 2012). Furthermore, the degree of Al-substitution may influence the HIRM of high-coercivity minerals (Liu et al., 2007), a factor that cannot be evaluated with our data set.

Paleoenvironmental and paleoclimatological implications

Last interglacial (MIS 5e)

As discussed in "Stratigraphy and Age Control of the Chenarli Profile," the well-developed paleosol (Btb horizon) of LU 7 almost certainly formed during MIS 5e. Occasional charcoal finds in this paleosol provide evidence for burning and might suggest warm and dry months within MIS 5e in the area, comparable with current natural summer fires in the NILP. Furthermore, during dry months, microbial organic matter decomposition increases, soil pH tends to be more alkaline due to evapotranspiration, and the oxygen diffusion rate increases (White et al., 1999). Hence, under oxic conditions (during dry months) in which evapotranspiration exceeds precipitation, both SP and SD grains form. In contrast, we postulate that dominant rainfall during wet seasons in MIS 5e resulted in carbonate leaching and lower soil pH, with clay accumulation and Fe mottling in the Btb horizon of LU 7. This produced stagnant conditions accompanied by a sharp depletion of dissolved oxygen in which SP particles may dissolve because of their smaller sizes and higher surface area to volume ratio, but SD particles are preserved (Yamazaki et al., 2003). This may explain why the χ_{fd}% of the Btb horizon of LU 7 is low, while χ_{ARM}/IRM values in this paleosol are high (Fig. 7).

Magnetite dissolution is widespread in gleyed soils (e.g., Dearing et al., 1996; Maher, 1998; Guo et al., 2001; Chlachula, 2003; Blundell et al., 2009; Roberts, 2015) and has also been observed in the strongly developed paleosols with Btb horizons that formed in MIS 5e at Mobarakabad, Toshan, and Neka-Abelou in the NFAM. These MIS 5e paleosols have lower magnetic susceptibilities (χ_{lf} and χ_{fd}%) than the overlying paleosols (Ghafarpour et al., 2016; Vlaminck et al., 2018; Kehl et al., 2021). Magnetic depletion is also observed in the Btb horizon of the MIS 5e paleosol of loess–paleosol sequences in the Czech Republic in which coarse-grained ferrimagnets were preserved, while pedogenic conditions were not favorable for the production and/or preservation of fine and ultrafine magnetic grains (Oches and Banerjee, 1996). Such a lack of correlation between χ_{lf} and degree of pedogenesis and paleoprecipitation has also been observed in magnetically depleted paleosols of Chinese loess deposits (e.g., Guo et al., 2001; Han et al., 2020). Considering the fact that precipitation patterns in the Czech Republic and China are distinctly different from those of northern Iran, we hypothesize that the magnetic depletion in these paleosols was controlled mainly by intense pedogenesis under excessive soil moisture conditions that changed soil redox conditions, rather than rainfall seasonality.

https://doi.org/10.1017/qua.2023.5 Published online by Cambridge University Press

The absence of a well-developed MIS 5e paleosol with Btb horizon at the Aghband section (Fig. 9) in the northern NILP (Fig. 1) compared with Neka-Abelou, Toshan, Mobarakabad, and Chenarli is consistent with the pronounced modern north–south gradient from (semi)arid to subhumid climates. This supports the idea that similar climatic gradients may have existed during paleosol formation in the NFAM and NILP (Khormali and Kehl, 2011; Khormali et al., 2020; Kehl et al., 2021). However, during MIS 5e, the eastern NILP experienced more humid conditions than in the Holocene, which is reflected in formation of a well-developed Btb horizon in LU 7 at Chenarli compared with weakly developed Bw and Bk horizons of the modern soil in LU 1.

Periods of loess deposition and pedogenesis from MIS 5d to the Holocene

The presence of gypsum and soluble salts in the Ckyz horizon of LU 4 indicates that gypsum and soluble salts were not leached after deposition, which suggests that loess accumulated under dry climates during MIS 5b (Fig. 3). Similarly, LCH of LU 5 and LU 6 are characterized by salt and gypsum accumulation and preservation. The gypsum presence in the LCH of all loess units was probably sourced from the nearby Kopet Dagh marly structures (Karimi et al., 2009; Lauer et al., 2017b). The sources of soluble salts in the LCH of LU 4–LU 6 may relate to terrestrial sediments enriched by salts during the late Khazarian transgression epoch between 130 and 76 ka (Yanina, 2012; Tudryn et al., 2013). A further assumption is that non-glacial erosion of nearby tectonically active mountains (Alborz and Kopet Dagh) produced fine silt-sized sediment in the area that was then carried into dry basins by fluvial transport of seasonal rivers (Ghafarpour et al., 2021b). Under this scenario, further silt-sized particles can be produced by salt weathering in dry basins (Smith et al., 2002; Muhs, 2007), where silts can be deflated easily to become dust that formed the salt-rich LCH (Ckyz and Cyz horizons; see Fig 3) in LU 4 to LU6.

The fact that the paleosols of LU 4 and LU 5 have the highest χ_{lf} and χ_{fd}% (Fig. 4) may reflect the formation of these paleosols in MIS 5a and 5c, respectively (Fig. 9), in accordance with previous reports of high χ_{lf} and χ_{fd}% values in MIS 5a and 5c paleosols in northern Iranian loess–paleosol sequences (Vlaminck et al., 2018; Kehl et al., 2021). Based on this correlation, which is supported by luminescence ages of 89.6 ± 6.4 ka and 130 ± 9.1 ka for samples CHE-3866 and CHE-3870, respectively, the Cky horizon of LU 3 probably started to accumulate with the onset of MIS 4 and the Ckyz horizon of LU 6 may indicate a loess depositional episode during MIS 5d.

The paleosol in LU 3 indicates a period of pedogenesis before ca. 30.8 ± 2.5 ka, probably during early-middle MIS 3 (Fig. 9). The timing of this period of pedogenesis may be comparable with paleosol formation during MIS 3 at Neka-Abelou (~49.3 to 40.4 ka), Toshan (~44.1 to 39.1 ka), and Mobarakabad (~46.8 to 34.4 ka) in the NFAM (Fig. 9) and with loess records from the lower Danube basin (Markovic et al., 2008; Fitzsimmons et al., 2012), western central Europe (Fischer et al., 2019), some Eurasian loess records (e.g., Dodonov et al., 2006; Rousseau et al., 2017; Hlavatskyi and Bakhmutov, 2021), and the Remizovka loess section in central Asia (Fitzsimmons et al., 2018). The sequence at Chenarli thus corroborates the notion of multiple loess depositional episodes separated by pedogenesis during MIS 3 in northern Iran.

Deposition of loess (Cy2 horizon of LU 2) on top of the paleosol of LU 3 may have been coeval with loess accumulation between ~40.4 and 28 ka at Neka-Abelou, ~44.1 and 29.7 ka at Toshan, and partially with loess deposition after 34.4 ka in the Mobarakabad and Aghband sections (Fig. 9). The presence of carbonate and gypsum and charcoal pieces (Fig. 3) in the Cky2 horizon of LU 2 (~10.3 m below the surface) provides evidence of dry conditions and a natural fire in the NILP. Luminescence ages of LU 2 confirm that loess deposition continued into the late MIS 2 (16.5 ± 1.5 ka). Therefore, our data and emerging chronologies from other loess records in northern Iran and semiarid central Asian loess sites (cf. the Remizovka and Maibulak sections in Kazakhstan; Fitzsimmons et al., 2018) indicate that significant loess accumulation took place during middle-late MIS 3.

The LGM loess in LU 2 (Cy1 and Cky1 horizons) at Chenarli correlates well with loess deposition between ~25.1 and 22.4 ka at Toshan. An LGM loess was not detected in the Neka-Abelou, Mobarakabad, and Aghband sections due to the lack of age control, but this period of dust accumulation was detected in previous dating (Frechen et al., 2009). The LGM depositional phase in Chenarli and Toshan is consistent with dating of loess elsewhere in Eurasia, with peak loess accumulation during the LGM (e.g., Antoine et al., 2009; Stevens et al., 2013; Fitzsimmons and Hambach, 2014; Fitzsimmons et al., 2018), and is also consistent with the widely accepted model for colder, drier climates at this time in central Asia (Ding et al., 2002; Vandenberghe et al., 2006; Machalett et al., 2008) and with a clearly defined LGM dust flux peak in the Chinese Loess Plateau (Kang et al., 2015). The period of pedogenesis (Bwb horizon of LU 2) during late MIS 2 at Chenarli (Fig. 9) was not observed in the Neka-Abelou, Toshan, Mobarakabad, and Aghband sections because of topographic effects, hillslope soil erosion, and/or insufficient age control in these loess records. In contrast, comparable paleosols are observed in loess–paleosol sequences at Stayky (ca. 16.4 ± 1.6 ka) and Roksolany (R-S1 pedocomplex [Dofinivka interstadial]) in Ukraine (Rousseau et al., 2011; Hlavatskyi and Bakhmutov, 2020), and Nilka and KS15-05 sections in the Ili Basin, central Asia (Yang et al., 2014; Wang et al., 2019).

The loess depositional phase (Cy horizon) in LU 1 may coincide with the Younger Dryas chronozone and is potentially coeval with arid conditions and the spreading of desert and steppe vegetation before 11.5 ka, inferred from pollen analyses of a deep-marine sediment core from the south basin of the Caspian Sea (Leroy et al., 2013). Similarly dry conditions with high dust flux and desert vegetation during the Younger Dryas were reported for loess records from Xinjiang, China, and southern Tajikistan (Chen et al., 2016; Yang et al., 2020).

CONCLUSIONS

The loess–paleosol sequence at Chenarli provides detailed insights into Late Quaternary environmental change in northeastern Iran. Positive correlation between the hematite DRS peaks, S-ratios, and χ_{fd}% values in the modern soil and paleosols suggest pedogenic formation of several iron minerals, including magnetite, maghemite, and hematite. The NILP during the last interglacial (MIS 5e) experienced higher precipitation than during the Holocene. High χ_{ARM}/IRM, but low χ_{lf} and χ_{fd}% values in the well-developed MIS 5e paleosol suggest that SD particles are preserved in preference to SP particles under reducing conditions due to size selectivity, leading to magnetic depletion in this paleosol. The low HIRM values in the well-developed LU 7 paleosol imply that HIRM cannot be interpreted simply in terms of the absolute concentration of magnetically hard minerals. MIS 5b loess deposition

https://doi.org/10.1017/qua.2023.5 Published online by Cambridge University Press

at ca. 89.6 ± 6.4 ka is associated with dry conditions, deduced from the presence of carbonate, gypsum, and soluble salts in the Ckyz horizon of LU 4. Comparison of our data with other paleoenvironmental records indicates that the period of pedogenesis in LU 3 may correlate to MIS 3, for which pedogenesis is documented in other northern Iranian, European, and central Asian loess records. Loess accumulation in Chenarli increased overall before ca. 30.8 ± 2.5 ka, peaked during the LGM, and continued until around ca. 16.5 ± 1.5 ka, which may have been coeval with substantially increased loess accumulation between 38 and 18 ka in central Asia.

Acknowledgments. This study is a part of the PhD thesis done at Gorgan University of Agricultural Sciences and Natural Resources, Iran. This work is based upon research funded by the Iran National Science Foundation (INSF) under the project no. 99006758. We thank Kathrin Worm for ARM and IRM measurements and Daniel Maxbauer for helpful discussion. The constructive comments of reviewers Christoph E. Geiss, Dmytro Hlavatskyi, Andrew P. Roberts, and Pengxiang Hu and editors Jaime Urrutia Fucugauchi and Derek Booth on previous versions of the article are highly appreciated.

REFERENCES

Ahmed, I.A., Maher, B.A., 2018. Identification and paleoclimatic significance of magnetite nanoparticles in soils. *Proceedings of the National Academy of Sciences USA* **115**, 1736–1741.

Antoine, P., Rousseau, D.D., Moine, O., Kunesch, S., Hatte, C., Lang, A., Tissoux, H., Zöller, L., 2009. Rapid and cyclic aeolian deposition during the Last Glacial in European loess: a high-resolution record from Nussloch, Germany. *Quaternary Science Reviews* **28**, 2955–2973.

Balsam, W., Ji, J., Chen, J., 2004. Climatic interpretation of the Luochuan and Lingtai loess sections, China, based on changing iron oxide mineralogy and magnetic susceptibility. *Earth and Planetary Science Letters* **223**, 335–348.

Balsam, W.L., Damuth, J.E., 2000. Further investigations of ship-board vs. shore-based spectral data: implications for interpreting Leg 164 sediment composition. In: Paull, C.K., Matsumoto, R., Wallace, P., Dillon, W.P. (Eds.), *Proceedings of the Ocean Drilling Program, Scientific Results*. Vol. **164**. Ocean Drilling Program, College Station, TX, p. 313324.

Balsam, W.L., Deaton, B.C., 1991. Sediment dispersal in the Atlantic Ocean: evaluation by visible light spectra. *Reviews in Aquatic Sciences* **4**, 411–447.

Begét, J.E., 2001. Continuous Late Quaternary proxy climate records from loess in Beringia. *Quaternary Science Reviews* **20**, 499–507.

Beuselinck, L., Govers, G., Poesen, J., Degraer, G., Froyen, L., 1998. Grain-size analysis by laser diffractometry: comparison with the sieve pipette method. *Catena* **32**, 193–208.

Bilardello, D., Banerjee, S.K., Volk, M.W., Soltis, J.A., Penn, R.L., 2020. Simulation of natural iron oxide alteration in soil: conversion of synthetic ferrihydrite to hematite without artificial dopants, observed with magnetic methods. *Geochemistry, Geophysics, Geosystems* **20**, e2020GC009037.

Blundell, A., Dearing, J.A., Boyle, J.F., Hannam, J.A., 2009. Controlling factors for the spatial variability of soil magnetic susceptibility across England and Wales. *Earth-Science Reviews* **95**, 158–188.

Bradák, B., Seto, Y., Stevens, T., Újvári, G., Fehér, K., Költringer, C., 2021. Magnetic susceptibility in the European Loess Belt: new and existing models of magnetic enhancement in loess. *Palaeogeography, Palaeoclimatology, Palaeoecology* **569**, 110329.

Catt, J.A., 1991. Soils as indicators of Quaternary climatic change in mid-latitude regions. *Geoderma* **51**, 167–187.

Chen, F.H., Jia, J., Chen, J.H., Li, G.Q., Zhang, X.J., Xie, H.C., Xia, D.S., Huang, W., 2016. Persistent Holocene wetting trend with the wettest Late-Holocene in the arid central Asia evidenced by loess–palaeosol sequence in Xinjiang, China. *Quaternary Science Reviews* **146**, 134–146.

Chepalyga, A.L., 2007. The late glacial great flood in the Ponto-Caspian basin. In: Yanko-Hombach, V.V., Gilbert, A.S., Panin, N., Dolukhanov, P.M. (Eds.), *The Black Sea Flood Question: Changes in Coastline, Climate and Human Settlement*. Springer, New York, pp. 119–148.

Chlachula, J., 2003. The Siberian loess record and its significance for reconstruction of Pleistocene climate change in north-central Asia. *Quaternary Science Reviews* **22**, 1879–1906.

Cornell, R.M., Schwertmann, U., 2003. *The Iron Oxides: Structure, Properties, Reactions, Occurrences and Uses*. Wiley-VCH, Weinheim.

Dearing, J.A., Hay, K.L., Baban, S.M.J., Huddleston, A.S., Wellington, E.M.H., Loveland, P.J., 1996. Magnetic susceptibility of soil: an evaluation of conflicting theories using a national data set. *Geophysical Journal International* **127**, 728–734.

Deaton, B.C., Balsam, W.L., 1991. Visible spectroscopy: a rapid method for determining hematite and goethite concentration in geological materials. *Journal of Sedimentary Petrology* **61**, 628–632.

Deng, C.L., Zhu, R.X., Jackson, M.J., Verosub, K.L., Singer, M.J., 2001. Variability of the temperature-dependent susceptibility of the Holocene eolian deposits in the Chinese loess plateau: a pedogenesis indicator. *Physics and Chemistry of the Earth, Part A: Solid Earth and Geodesy* **26**, 873–878.

Ding, Z.L., Ranov, V., Yang, S.L., Finaev, A., Han, J.M., Wang, G.A., 2002. The loess record in southern Tajikistan and correlation with Chinese loess. *Earth and Planetary Science Letters* **200**, 387–400.

Dodonov, A.E., Sadchikova, T.A., Sedov, S.N., Simakova, A.N., Zhou, L.P., 2006. Multidisciplinary approach for paleoenvironmental reconstruction in loess-paleosol studies of the Darai Kalon section, Southern Tajikistan. *Quaternary International* 152–153, 48–58.

Eckmeier, E., Egli, M., Schmidt, M.W.I., Schlumpf, N., N?tzli, M., Minikus-Stary, N., Hagedorn, F., 2013. Preservation of fire-derived carbon compounds and sorptive stabilisation promote the accumulation of organic matter in black soils of the Southern Alps. *Geoderma* **159**, 147–155.

Evans, M.E., Heller, F., 2003. *Environmental Magnetism; Principles and Applications of Enviromagnetics*. Academic Press, San Diego, CA.

Fischer, P., Hambach, U., Klasen, N., Schulte, P., Zeeden, C., Steininger, F., Lehmkuhl, F., Gerlach, R., Radtke, U., 2019. Landscape instability at the end of MIS 3 in western Central Europe: evidence from a multi proxy study on a loess-palaeosol-sequence from the eastern Lower Rhine Embayment, Germany. *Quaternary International* **502**, 119–136.

Fitzsimmons, K.E., Hambach, U., 2014. Loess accumulation during the last glacial maximum: evidence from Urluia, Southeastern Romania. *Quaternary International* 334–335, 74–85.

Fitzsimmons, K.E., Marković, S.B., Hambach, U., 2012. Pleistocene environmental dynamics recorded in the loess of the middle and lower Danube basin. *Quaternary Science Reviews* **41**, 104–118.

Fitzsimmons, K.E., Sprafke, T., Zielhofer, C., Günter, C., Deom, J.M., Sala, R., Iovita, R., 2018. Loess accumulation in the Tian Shan piedmont: implications for palaeoenvironmental change in arid Central Asia. *Quaternary International* **469**, 30–43.

Frechen, M., Kehl, M., Rolf, C., Sarvati, R., Skowronek, A., 2009. Loess chronology of the Caspian Lowland in Northern Iran. *Quaternary International* **198**, 220–233.

Geiss, C.E., 2014. Does timing or location matter? The influence of site variability and short-term variations in precipitation on magnetic enhancement in loessic soils. *Geoderma* 230–231, 280–287.

Geiss, C.E., Egli, R., Zanner, C.W., 2008. Direct estimates of pedogenic magnetite as a tool to reconstruct past climates from buried soils. *Journal of Geophysical Research. Solid Earth* **113**, 1–15.

Geiss, C.E., Zanner, C.W., 2006. How abundant is pedogenic magnetite? Abundance and grain size estimates for loessic soil based on rock magnetic analyses. *Journal of Geophysical Research* **111**, 1–19.

Geiss, C.E., Zanner, C.W., 2007. Sediment magnetic signature of climate in modern loessic soils from the Great Plains. *Quaternary International* 162–163, 97–110.

Ghafarpour, A., Khormali, F., Balsam, W., Forman, S.L., Cheng, L., Song, Y., 2021a. The formation of iron oxides and magnetic enhancement mechanisms in northern Iranian loess-paleosol sequences: evidence from diffuse reflectance spectrophotometry and temperature dependence of magnetic susceptibility. *Quaternary International* **589**, 68–82.

Ghafarpour, A., Khormali, F., Balsam, W., Karimi, A., Ayoubi, S., 2016. Climatic interpretation of loess-paleosol sequences at Mobarakabad and Aghband, northern Iran. *Quaternary Research* **86**, 95–109.

https://doi.org/10.1017/qua.2023.5 Published online by Cambridge University Press

Ghafarpour, A., Khormali, F., Forman, S. L., 2017. *The OSL chronology of the loess-paleosol sequence Mobarakabad, northern Iran*. In LoessFest 2017, Gorgan, Iran, 8–12 October, pp. 68–69.

Ghafarpour, A., Khormali, F., Meng, X., Tazikeh, H., 2021b. Late Pleistocene climate and dust source from the Mobarakabad loess–paleosol sequence, northern foothills of the Alborz Mountains. *Frontiers in Earth Science* **9**, 1–16.

Guo, B., Zhu, R.X., Roberts, A.P., Florindo, F., 2001. Lack of correlation between paleoprecipitation and magnetic susceptibility of Chinese loess/paleosol sequences. *Geophysical Research Letters* **28**, 4259–4262.

Han, Y., Liu, X., Zhao, G., Zhang, Z., Lü, B., Chen, Q., 2020. Magnetic characteristics of Guangshan loess from northern piedmont of Dabie Mountains, east-central China. *Geophysical Journal International* **222**, 1213–1223.

He, T., Liu, L., Chen, Y., Sheng, X., Ji, J., Chen, J., 2018. Glacial–interglacial change in chlorite concentration from the Lingtai Section in the Chinese Loess Plateau over the past 1.2 Ma and its possible forcing mechanisms. *Quaternary Research* **89**, 511–519.

Heller, F., Liu, T.S., 1984. Magnetism of Chinese loess deposits. *Geophysical Journal International* **77**, 125–141.

Heslop, D., 2009. On the statistical analysis of the rock magnetic S-ratio. *Geophysical Journal International* **178**, 159–161.

Hlavatskyi, D., Bakhmutov, V., 2021. Early–Middle Pleistocene magnetostratigraphic and rock magnetic records of the Dolynske Section (lower Danube, Ukraine) and their application to the correlation of loess–palaeosol sequences in eastern and south-eastern Europe. *Quaternary* **4**(4), 43.

Hlavatskyi, D.V., Bakhmutov, V.G., 2020. Magnetostratigraphy and magnetic susceptibility of the best developed Pleistocene loess-palaeosol sequences of Ukraine: implications for correlation and proposed chronostratigraphic models. *Geological Quarterly*, **64**. https://doi.org/10.7306/gq.1544

Hrouda, F., 1994. A technique for the measurements of thermal changes of magnetic susceptibility of weakly magnetic rocks by the CS-2 apparatus and KLY-2 Kappabridge. *Geophysical Journal International* **118**, 604–612.

Hu, P., Jiang, Z., Liu, Q., Heslop, D., Roberts, A. P., Torrent, J., Barrón, V., 2016. Estimating the concentration of aluminum-substituted hematite and goethite using diffuse reflectance spectrometry and rock magnetism: feasibility and limitations. *Journal of Geophysical Research: Solid Earth* **121**, 4180–4194.

Hu, P., Liu, Q., Heslop, D., Roberts, A.P., Jin, C., 2015. Soil moisture balance and magnetic enhancement in loess–paleosol sequences from the Tibetan Plateau and Chinese Loess Plateau. *Earth and Planetary Science Letters* **409**, 120–132.

Hu, P.X., Liu, Q.S., Torrent, J., Barrón, V., Jin, C., 2013. Characterizing and quantifying iron oxides in Chinese loess/paleosols: implications for pedogenesis. *Earth and Planetary Science Letters* 369–370, 271–283.

Hu, X.F., Du, Y., Guan, C.L., Xue, Y., Zhang, G.L., 2014. Color variations of the Quaternary Red Clay in southern China and its paleoclimatic implications. *Sedimentary Geology* **303**, 15–25.

Huntley, D.J., Lamothe, M., 2001. Ubiquity of anomalous fading in K-feldspars and the measurement and correction for it in optical dating. *Canadian Journal of Earth Sciences* **38**, 1093–1106.

Hyodo, M., Sano, T., Matsumoto, M., Seto, Y., Bradák, B., Suzuki, K., Fukuda, J.I., Shi, M., Yang, T., 2020. Nanosized authigenic magnetite and hematite particles in mature-paleosol phyllosilicates: new evidence for a magnetic enhancement mechanism in loess sequences of China. *Journal of Geophysical Research: Solid Earth* **125**, e2019JB018705.

Ji, J., Balsam, W., Chen, J., Liu, L., 2002. Rapid and quantitative measurement of hematite and goethite in the Chinese loess-paleosol sequence by diffuse reflectance spectroscopy. *Clays and Clay Minerals* **50**, 208–216.

Jiang, Z., Liu, Q., Roberts, A.P., Dekkers, M.J., Barrón, V., Torrent, J., Li, S., 2022. The magnetic and color reflectance properties of hematite: from Earth to Mars. *Reviews of Geophysics* **60**, e2020RG000698.

Judd, D.B., Wyszecki, G., 1975. *Color in Business, Science, and Industry*. Wiley, New York, p. 553.

Kang, S., Roberts, H.M., Wang, X., An, Z., Wang, M., 2015. Mass accumulation rate changes in Chinese loess during MIS 2, and asynchrony with records from Greenland ice cores and North Pacific Ocean sediments during the Last Glacial Maximum. *Aeolian Research* **19** (Part B), 251–258.

Karimi, A., Frechen, M., Khademi, H., Kehl, M., Jalalian, A., 2011. Chronostratigraphy of loess deposits in northeast Iran. *Quaternary International* **234**, 124–132.

Karimi, A., Khademi, H., Ayoubi, S., 2013. Magnetic susceptibility and morphological characteristics of a loess–paleosol sequence in northeastern Iran. *Catena* **101**, 56–60.

Karimi, A., Khademi, H., Kehl, M., Jalalian, A., 2009. Distribution, lithology and provenance of peridesert loess deposits in northeastern Iran. *Geoderma* **148**, 241–250.

Kehl, M., 2010. *Quaternary Loesses, Loess-Like Sediments, Soils and Climate Change in Iran*. Relief, Boden, Paläoklima 24. Gebr. Borntraeger Science Publishers, Stuttgart, p. 208.

Kehl, M., Vlaminck, S., Köhler, T., Laag, C., Rolf, C., Tsukamoto, S., Frechen, M., Sumita, M., Schmincke, H.U., Khormali, F., 2021. Pleistocene dynamics of dust accumulation and soil formation in the southern Caspian Lowlands—new insights from the loess-paleosol sequence at Neka-Abelou, northern Iran. *Quaternary Science Reviews* **253**, 106774.

Khormali, F., Kehl, M., 2011. Micromorphology and development of loess-derived surface and buried soils along a precipitation gradient in northern Iran. *Quaternary International* **234**, 109–123.

Khormali, F., Shahriari, A., Ghafarpour, A., Kehl, M., Lehndorff, E., Frechen, M., 2020. Pedogenic carbonates archive modern and past precipitation change—a transect study from soils and loess-paleosol sequences from northern Iran. *Quaternary International* **552**, 79–90.

Költringer, C., Stevens, T., Bradák, B., Almqvist, B., Kurbanov, R., Snowball, I., Yarovaya, S., 2021. Enviromagnetic study of Late Quaternary environmental evolution in Lower Volga loess sequences, Russia. *Quaternary Research* **103**, 49–73.

Költringer, C., Stevens, T., Lindner, M., Baykal, Y., Ghafarpour, A., Khormali, F., Taratunina, N., Kurbanov, R., 2022. Quaternary sediment sources and loess transport pathways in the Black Sea–Caspian Sea region identified by detrital zircon U-Pb geochronology. *Global and Planetary Change* **209**, 103736.

Krijgsman, W., Tesakov, A., Yanina, T., Lazarev, S., Danukalova, G., Van Baak, C.G.C., Agustí, J., *et al.*, 2019. Quaternary time scales for the Pontocaspian domain: interbasinal connectivity and faunal evolution. *Earth-Science Reviews* **188**, 1–40.

Kukla, G., An, Z., 1989. Loess stratigraphy in central China. *Palaeogeography, Palaeoclimatology, Palaeoecology* **72**, 203–225.

Laag, C., Hambach, U., Zeeden, C., Lagroix, F., Guyodo, Y., Veres, D., Jovanović, M., Marković, S., 2021. A detailed paleoclimate proxy record for the middle Danube Basin over the last 430 kyr: a rock magnetic and colorimetric study of the Zemun loess–paleosol sequence. *Frontiers in Earth Science* **9**, 600086.

Lauer, T., Frechen, M., Vlaminck, S., Kehl, M., Lehndorff, E., Shahriari, A., Khormali, F., 2017a. Luminescence-chronology of the loess palaeosol sequence Toshan, northern Iran—a highly resolved climate archive for the last glacial–interglacial cycle. *Quaternary International* **429**, 3–12.

Lauer, T., Vlaminck, S., Frechen, M., Rolf, C., Kehl, M., Sharifi, J., Lehndorff, E., Khormali, F., 2017b. The Agh Band loess-palaeosol sequence e a terrestrial archive for climatic shifts during the last and penultimate glacial-interglacial cycles in a semiarid region in northern Iran. *Quaternary International* **429**, 13e30.

Leroy, S.A.G., Kakroodi, A.A., Kroonenberg, S., Lahijani, H.K., Alimohammadian, A., Nigarov, A., 2013. Holocene vegetation history and sea level changes in the SE corner of the Caspian Sea: relevance to SW Asia climate. *Quaternary Science Reviews* **70**, 28–47.

Leroy, S.A.G., Lahijani, H.A.K., Crétaux, J.-F., Aladin, N.V., Plotnikov, I.S., 2020. Past and current changes in the largest lake of the world: the Caspian Sea. In: Mischke, S. (Ed.), *Large Asian Lakes in a Changing World. Natural State and Human Impact. Springer*, Cham, Switzerland, pp. 65–107. DOI: 10.1007/978-3-030-42254-7_3

Liu, Q., Roberts, A.P., Torrent, J., Horng, C.-S., Larrasoaña, J.C., 2007. What do the HIRM and S-ratio really measure in environmental magnetism? *Geochemistry, Geophysics, Geosystems* **8**, Q09011.

Machalett, B., Oches, E.A., Zöller, L., Hambach, U., Mavlyanova, N.G., Markovic, S., 2008. Aeolian dust dynamics in central Asia during the Pleistocene: driven by the long-term migration, seasonality, and

https://doi.org/10.1017/qua.2023.5 Published online by Cambridge University Press

permanency of the Asiatic polar front. *Geochemistry, Geophysics, Geosystems* **9**, 1–22.

Maher, B.A., 1998. Magnetic properties of modern soils and Quaternary loessic paleosols: paleoclimatic implications. *Palaeogeography, Palaeoclimatology, Palaeoecology* **137**, 25–54.

Maher, B.A., MengYu, H., Roberts, H.M., Wintle, A.G., 2003. Holocene loess accumulation and soil development at the western edge of the Chinese Loess Plateau. Implications for magnetic proxies of palaeorainfall. *Quaternary Science Reviews* **22**, 445.

Markovic, S.B., Bokhorst, M.P., Vandenberghe, J., McCoy, W.D., Oches, E.A., Hambach, U., Gaudenyi, T., *et al.*, B., 2008. Late Pleistocene loess-palaeosol sequences in the Vojvodina region, north Serbia. *Journal of Quaternary Science* **23**, 73–84.

Martinson, D.G., Pisias, N.G., Hays, J.D., Imbrie, J., Moore, T.C., Shackleton, N.J., 1987. Age dating and the orbital theory of the ice ages: development of a high-resolution 0 to 300,000-year chrono-stratigraphy. *Quaternary Research* **27**, 1–29.

Maxbauer, D.P., Feinberg, J.M., Fox, D.L., 2016. Magnetic mineral assemblages in soils and paleosols as the basis for paleoprecipitation proxies: a review of magnetic methods and challenges. *Earth-Science Reviews* **155**, 28–48.

Muhs, D.R., 2007. Loess deposits, origins, and properties. In: Elias, S. (Ed.), *The Encyclopedia of Quaternary Sciences*. Elsevier, Amsterdam, pp. 1405–1418.

Najafi, H., Karimi, A., Haghnia, G.H., Khormali, F., Ayoubi, S., Tazikeh, H., 2019. Paleopedology and magnetic properties of Sari loess-paleosol sequence in Caspian lowland, northern Iran. *Journal of Mountain Science* **16**, 1559–1570.

Oches, E.A., Banerjee, S.K., 1996. Rock-magnetic proxies of climate change from loess-paleosol sediments of the Czech Republic. *Studia Geophysica et Geodaetica* **40**, 287–300.

Orgeira, M.J., Egli, R., Compagnucci, R.H., 2011. A quantitative model of magnetic enhancement in loessic soils. In: Petrovsky, E., Ivers, D., Harinarayana, T., Herrero-Bervera, E. (Eds.), *Magnetic Earth's Interior*. Springer, Dordrecht, Netherlands, pp. 361–397.

Pecsi, M., 1995. Loess stratigraphy and Quaternary climatic change. In: Pécsi, M., Schweitzer, F. (Eds.), *Concept of Loess, Loess-Paleosol Stratigraphy*. Loess in Form 3. Geographical Research Institute, Hungarian Academy of Sciences, Budapest, pp. 23–30.

Peng, S., Hao, Q., Oldfield, F., Guo, Z., 2014. Release of iron from chlorite weathering and links to magnetic enhancement in Chinese loess deposits. *Catena* **117**, 43–49.

Pourmasoumi, M., Khormali, F., Ayoubi, S., Kehl, M., Kiani, F., 2019. Development and magnetic properties of loess-derived forest soils along a precipitation gradient in northern Iran. *Journal of Mountain Science* **16**, 1848–1868.

Quinton, E.E., Dahms, D.E., Geiss, C.E., 2012. Magnetic analyses of soils from the Wind River Range, Wyoming, constrain rates and pathways of magnetic enhancement for soils from semiarid climates. *Geochemistry Geophysics Geosystems* **12**, 1–16.

Rahimzadeh, N., Khormali, F., Gribenski, N., Tsukamoto, S., Kehl, M., Pint, A., Kiani, F., Frechen, M., 2019. Timing and development of sand dunes in the Golestan Province, northern Iran—implications for the Late-Pleistocene history of the Caspian Sea. *Aeolian Research* **41**, 100538.

Ramsey, C.B., 2017. Methods for summarizing radiocarbon datasets. *Radiocarbon* **59**, 1809–1833.

Reimer, P.J., Bard, E., Bayliss, A., Beck, J.W., Blackwell, P.G., Ramsey, C.B., Buck, C.E., *et al.*, 2013. IntCal13 and Marine13 radiocarbon age calibration curves 0–50,000 years cal BP. *Radiocarbon* **55**, 1869–1887.

Rethemeyer, J., Fülöp, R.H., Höfle, S., Wacker, L., Heinze, S., Hajdas, I., Patt, U., König, S., Stapper, B., Dewald, A., 2013. Status report on sample preparation facilities for 14C analysis at the new Cologne AMS center. *Nuclear Instruments and Methods in Physics Research Section B: Beam Interactions with Materials and Atoms* **294**, 168–172.

Roberts, A.P., 2015. Magnetic mineral diagenesis. *Earth-Science Reviews,* **151**, 1–47.

Roberts, A.P., Zhao, X., Heslop, D., Abrajevitch, A., Chen, Y.H., Hu, P., Jiang, Z., Liu, Q., Pillans, B.J., 2020. Hematite (α-Fe_2O_3) quantification in sedimentary magnetism: Limitations of existing proxies and ways forward. *Geoscience Letters* **7**, 8.

Robinson, S.G., 1986. The late Pleistocene palaeoclimatic record of North Atlantic deep-sea sediments revealed by magnetic mineral measurements. *Physics of the Earth and Planetary Interiors* **42**, 22–47.

Rousseau, D.D., Antoine, P., Boers, N., Lagroix, F., Ghil, M., Lomax, J., Fuchs, M., *et al.*, 2020. Dansgaard–Oeschger-like events of the penultimate climate cycle: the loess point of view. *Climate of the Past* **16**, 713–727.

Rousseau, D.D., Antoine, P., Gerasimenko, N., Sima, A., Fuchs, M., Hatte, C., Moine, O., Zoeller, L., 2011. North Atlantic abrupt climatic events of the last glacial period recorded in Ukrainian loess deposits. *Climate of the Past* **7**, 221–234.

Rousseau, D.D., Boers, N., Sima, A., Svensson, A., Bigler, M., Lagroix, F., Taylor, S., Antoine, P., 2017. (MIS3 & 2) millennial oscillations in Greenland dust and Eurasian aeolian records e a paleosol perspective. *Quaternary Science Reviews* **169**, 99–113.

Salvador, A., 1994. *International Stratigraphic Guide*. 2nd ed. Geological Society of America, Boulder, CO.

Sandeep, K., Shankar, R., Warrier, A.K., Balsam, W., 2017. Diffuse reflectance spectroscopy of a tropical southern Indian lake sediment core: a window to environmental change. *Episodes* **40**, 47–56.

Schaetzl, R.J., Bettis, E.A., Crouvi, O., Fitzsimmons, K.E., Grimley, D.A., Hambach, U., Lehmkuhl, F., *et al.*, 2018. Approaches and challenges to the study of loess—introduction to the LoessFest special issue. *Quaternary Research* **89**, 563–618.

Scheinost, A.C., Schwertmann, U., 1999. Color identification of iron oxides and hydroxysulfates: use and limitations. *Soil Science Society of America Journal* **63**, 1463–1471.

Sharifigarmdareh, J., Khormali, F., Scheidt, S., Rolf, C., Kehl, M., Frechen, M., 2020. Investigating soil magnetic properties with pedogenic variation along a precipitation gradient in loess-derived soils of the Golestan province, northern Iran. *Quaternary International* **552**, 100–110.

Singer, M.J., Verosub, K.L., Fine, P., TenPas, J., 1996. A conceptual model for the enhancement of magnetic susceptibility in soils. *Quaternary International* **34**, 243–248.

Smith, B.J., Wright, J.S., Whalley, W.B., 2002. Sources of non-glacial, loess-size quartz silt and the origins of "desert loess." *Earth-Science Reviews* **59**, 1–26.

Soil Survey Staff, 2014. *Keys to Soil Taxonomy*. U.S. Department of Agriculture, Natural Resources Conservation Service, Washington, DC.

Song, Y., Li, Y., Cheng, L., Zong, X., Kang, S., Ghafarpour, A., Li, X., *et al.*, 2021. Spatio-temporal distribution of Quaternary loess across Central Asia. *Palaeogeography, Palaeoclimatology, Palaeoecology* **567**, 110279.

Spassov, S., Heller, F., Kretzschmar, R., Evans, M.E., Yue, L.P., Nourgaliev, D.K., 2003. Detrital and pedogenic magnetic mineral phases in the loess/palaeosol sequence at Lingtai (Central Chinese Loess Plateau). *Physics of the Earth and Planetary Interiors* **140**, 255–275.

Stevens, T., Adamiec, G., Bird, A.F., Lu, H., 2013. An abrupt shift in dust source on the Chinese Loess Plateau revealed through high sampling resolution OSL dating. *Quaternary Science Reviews* **82**, 121e132.

Stevens, T., Sechi, D., Bradák, B., Orbe, R., Baykal, Y., Cossu, G., Tziavaras, C., Andreucci, S., Pascucci, V., 2020. Abrupt last glacial dust fall over southeast England associated with dynamics of the British-Irish ice sheet. *Quaternary Science Reviews* **250**, 106641.

Sun, W., Banerjee, S.K., Hunt, C.P., 1995. The role of maghemite in the enhancement of magnetic signal in the Chinese loess-paleosol sequence: an extensive rock magnetic study combined with citrate-bicarbonate-dithionite treatment. *Earth and Planetary Science Letters* **133** (3e4), 493e505.

Tecsa, V., Mason, J.A., Johnson, W.C., Miao, X., Constantin, D., Radu, S., Magdas, D.A., Veres, D., Marković, S.B., Timar-Gabor, A., 2020. Latest Pleistocene to Holocene loess in the central Great Plains: optically stimulated luminescence dating and multi-proxy analysis of the Enders loess section (Nebraska, USA). *Quaternary Science Reviews* **229**, 106130.

Thompson, R., Oldfield, F., 1986. *Environmental Magnetism*. Allen and Unwin, Winchester, MA.

https://doi.org/10.1017/qua.2023.5 Published online by Cambridge University Press

Torrent, J., Liu, Q., Bloemendal, J., Barrón, V., 2007. Magnetic enhancement and iron oxides in the upper Luochuan loess–paleosol sequence, Chinese Loess Plateau. *Soil Science Society of America Journal* **71**, 1570–1578.

Tudryn, A., Chalié, F., Lavrushin, Yu.A., Antipov, M.P., Spiridonova, E.A., Lavrushin, V., Tucholka, P., Leroy, S.A.G., 2013. Late Quaternary Caspian Sea environment: late Khazarian and Early Khvalynian transgressions from the lower reaches of the Volga river. *Quaternary International* **292**, 193–204.

Vandenberghe, J., Renssen, H., van Huissteden, K., Nugteren, G., Konert, M., Lu, H., Dodonov, A., Buylaert, J.-P., 2006. Penetration of Atlantic westerly winds into central and East Asia. *Quaternary Science Reviews* **25**, 2380–2389.

Vlaminck, S., Kehl, M., Lauer, T., Shahriari, A., Sharifi, J., Eckmeier, E., Lehndorff, E., Khormali, F., Frechen, M., 2016. Loess-soil sequence at Toshan (northern Iran): insights into late Pleistocene climate change. *Quaternary International* **399**, 122–135.

Vlaminck, S., Kehl, M., Rolf, C., Franz, S.O., Lauer, T., Lehndorff, E., Frechen, M., Khormali, F., 2018. Late Pleistocene dust dynamics and pedogenesis in Southern Eurasia— detailed insights from the loess profile Toshan (NE Iran). *Quaternary Science Reviews* **180**, 75–95.

Wacha, L., Laag, C., Grizelj, A., Tsukamoto, S., Zeeden, C., Ivanišević, D., Rolf, C., Banak, A., Frechen, M., 2021. High-resolution palaeoenvironmental reconstruction at Zmajevac (Croatia) over the last three glacial/interglacial cycles. *Palaeogeography, Palaeoclimatology, Palaeoecology* **576**, 110504.

Wang, L., Jia, J., Xia, D., Liu, H., Gao, F., Duan, Y., Wang, Q., Xie, H., Chen, F., 2019. Climate change in arid central Asia since MIS 2 revealed from a loess sequence in Yili Basin, Xinjiang, China. *Quaternary International* **502**, 258–266.

Wang, X., Wei, H.T., Taheri, M., Khormali, F., Danukalova, G., Chen, F.H., 2016. Early Pleistocene climate in western arid central Asia inferred from loess-palaeosol sequences. *Scientific Reports* **6**, 20560.

White, A.F., Blum, A.E., Bullen, T.D., Vivit, D.V., Schulz, M., Fitzpatrick, J., 1999. The effect of temperature on experimental and natural chemical weathering rates of granitoid rocks. *Geochimica et Cosmochimica Acta* **63**, 3277–3291.

Worm, H.U., 1998. On the superparamagnetic-stable single domain transition for magnetite and frequency dependency of susceptibility. *Geophysical Journal International* **133**, 201–206.

Yamazaki, T., Abdeldayem, A.L., Ikehara, K., 2003. Rock-magnetic changes with reduction diagenesis in Japan Sea sediments and preservation of geomagnetic secular variation in inclination during the last 30,000 years. *Earth, Planets and Space* **55**, 327–340.

Yang, S., Forman, S.L., Song, Y., Pierson, J., Mazzocco, J., Li, X., Shi, Z., Fang, X., 2014. Evaluating OSL-SAR protocols for dating quartz grains from the loess in Ili Basin, Central Asia. *Quaternary Geochronology* **20**, 78–88.

Yang, S., Li, D., Liu, N., Zan, J., Liu, W., Kang, J., Murodov, A., Fang, X., 2020. Quartz optically stimulated luminescence dating of loess in Tajikistan and its paleoclimatic implications for arid Central Asia since the Lateglacial. *Palaeogeography, Palaeoclimatology, Palaeoecology* **556**, 109881.

Yanina, T.A., 2012. Correlation of the Late Pleistocene paleogeographical events of the Caspian Sea and Russian Plain. *Quaternary International* **271**, 120–129.

Yanina, T.A., 2014. The Ponto-Caspian region: environmental consequences of climate change during the Late Pleistocene. *Quaternary International* **345**, 88–99.

Yanina, T., Sorokin, V., Bezrodnykh, Y., Romanyuk, B., 2018. Late Pleistocene climatic events reflected in the Caspian Sea geological history (based on drilling data). *Quaternary International* **465**, 130–141.

Ye, C., Yang, Y., Fang, X., Zan, J., Tan, M., Yang, R., 2020. Chlorite weathering linked to magnetic enhancement in red clay on the Chinese Loess Plateau. *Palaeogeography, Palaeoclimatology, Palaeoecology* **538**, 109446.

Zeeden, C., Hambach, U., Veres, D., Fitzsimmons, K., Obreht, I., Bösken, J., Lehmkuhl, F., 2018. Millennial scale climate oscillations recorded in the Lower Danube loess over the last glacial period. *Palaeogeography, Palaeoclimatology, Palaeoecology* **509**, 164–181.

Zeeden, C., Krauß, L., Kels, H., Lehmkuhl, F., 2017. Digital image analysis of outcropping sediments: Comparison to photospectrometric data from Quaternary loess deposits at Şanovița (Romania) and Achenheim (France). *Quaternary International* **429**, 100–107.

https://doi.org/10.1017/qua.2023.5 Published online by Cambridge University Press